Electronics-free Passive Ultrasonic Communication Link for Deep-tissue Sensor Implants

by

Umut Can Yener

A Dissertation Submitted to the
Graduate School of Sciences and Engineering
in Partial Fulfillment of the Requirements for
the Degree of

Master of Science

in

Mechanical Engineering

KOÇ ÜNİVERSİTESİ

July 5, 2024

Electronics-free Passive Ultrasonic Communication Link for Deep-tissue Sensor Implants

Koç University

Graduate School of Sciences and Engineering

This is to certify that I have examined this copy of a master's thesis by

Umut Can Yener

and have found that it is complete and satisfactory in all respects,

and that any and all revisions required by the final

examining committee have been made.

Committee Members:

Assist. Prof. Levent Beker (Advisor)

Assist. Prof. Murat Kuşcu

Assist. Prof. Hasan Uluşan

Date:

To my loved ones...

ABSTRACT

Electronics-free Passive Ultrasonic Communication Link for Deep-tissue Sensor Implants
Umut Can Yener
Master of Science in Mechanical Engineering
July 5, 2024

Wireless communication technologies are critical for the non-invasive in-situ monitoring of vital signs in deep tissues. Wireless ultrasonic links demonstrated so far solved the shortcomings of electromagnetic wave-based communication methods. However, they either require highly customized and complex designs for the implant electronics or rely on physical changes in implanted metamaterials.

This thesis proposes a novel wireless ultrasonic communication method for implantable applications. The method utilizes a small piezoelectric material used as an antenna, connected to a capacitive sensor in parallel. The capacitive changes occurring in the integrated sensor cause the resonance characteristics of the antenna to change. These changes can be captured by ultrasound pulse-echo measurements conducted by a broadband interrogator ultrasonic transducer. Thus, a wireless and electronics-free ultrasonic communication link can be realized for deeply implanted capacitive sensors.

The ultrasonic antenna is designed based on the equivalent circuit modeling results. The bulk piezoceramic material selection is done considering the piezoelectric properties and availability. The fabricated antenna and the proposed communication method are characterized. Additionally, the antenna is integrated with a commercial capacitive pressure sensor and the proposed method is demonstrated in vitro at a depth of 5 cm in order to evaluate the systems's applicability using medically relevant pressures. The method demonstrates decent performance, with a maximum sensitivity of -236.2 Hz/pF.

The proposed communication method enables simple implant design and fabrication, eliminates the need for integrated circuits and power harvesting circuitry, and offers flexibility in terms of sensor integration since any capacitive sensor can be integrated into the system.

ÖZETÇE

Derin Doku Sensör İmplantları için Elektroniksiz Pasif Ultrasonik Haberleşme Kanalı
Umut Can Yener
Makine Mühendisliği, Yüksek Lisans
5 Temmuz 2024

Kablosuz haberleşme teknolojileri, derin dokulardaki hayati belirtilerin invazif olmayan yöntemler ile izlenmesi için kritik öneme sahiptir. Şimdiye kadar gösterilen kablosuz ultrasonik kanallar, elektromanyetik dalga tabanlı iletişim yöntemlerinin eksikliklerini çözmüştür, ancak bu teknolojiler ya implant elektroniğinde son derece özelleşmiş ve karmaşık bir tasarım gerektirir ya da vücut içine yerleştirilen meta-malzemelerdeki fiziksel değişikliklerin etkilerine dayanır.

Bu tez, implant edilebilir uygulamalar için yeni bir kablosuz ultrasonik haberleşme yöntemi önermektedir. Yöntem, bir anten olarak kullanılan küçük bir piezoelektrik malzeme ile paralel bağlanmış bir kapasitif sensörün kullanımını içermektedir. Entegre sensörde meydana gelen kapasitif değişiklikler, antenin rezonans özelliklerinin değişmesine neden olur. Bu değişiklikler, geniş bantlı bir ultrasonik dönüştürücü tarafından gerçekleştirilen ultrasonik darbe-yankı ölçümleri ile yakalanabilir. Böylece, derin implant edilmiş kapasitif sensörler için kablosuz ve elektroniğe ihtiyaç duymayan bir ultrasonik haberleşme kanalı gerçekleştirilebilir.

Ultrasonik anten, eşdeğer devre modelleme sonuçlarına dayalı olarak tasarlanmıştır. Yığın piezoseramik malzeme seçimi piezoelektrik özellikler ve erişilebilirlik göz önünde bulundurularak yapılmıştır. İmal edilen anten ve önerilen haberleşme yöntemi karakterize edilmiştir. Buna ek olarak sistemin uygulanabilirliğini değerlendirmek amacıyla, üretilen anten ticari bir kapasitif basınç sensörü ile entegre edilmiş ve önerilen haberleşme yöntemi bir deney düzeneği içinde (in vitro), tıbbi uygulama basınçları kullanılarak 5 cm derinlikte gösterilmiştir. Yöntem, -236.2 Hz/pF maksimum hassasiyet ile iyi bir performans sergilemektedir.

Önerilen haberleşme yöntemi, basit implant tasarımı ve üretimini mümkün kılıp, entegre devrelere ve güç toplama devrelerine olan ihtiyacı ortadan kaldırırken her türlü kapasitif sensörün sisteme entegre edilebilmesi açısından esneklik sunmaktadır.

ACKNOWLEDGMENTS

I would like to express my deepest gratitude to several individuals and facilities for their invaluable support and guidance throughout my M.S. journey at Koç University.

First, I would like to thank my advisor, Dr. Levent Beker, for his support and guidance. His encouragement has been instrumental in shaping the direction of my research and academic growth. I am truly grateful for the opportunities he provided.

I also would like to extend my heartfelt thanks to Dr. Emin Istif, Dr. Ritu Das, Abdulkadir Yasin Atik, Emine Bardakçı, Özgür Deniz Temel, Maide Miray Albay, Ecem Ezgi Özkahraman, Fariborz Mirlou, Taher Abbasiasl, and all other current and former members of the Biointegrated Micro Devices Laboratory for their friendship, collaboration, and the stimulating discussions that made my research experience enjoyable and fulfilling. A special mention to Alp Timuçin Toymuş for his exceptional academic and personal support; his friendship, assistance, and encouragement have been a cornerstone of my success.

I am especially grateful to Çiğdem Buse Oral for her unwavering understanding, support, and encouragement during the most difficult parts of my M.S. journey. She has been a constant source of strength for me, and her patience and love have been invaluable. Words cannot describe how grateful and lucky I feel to have her by my side. Her belief in me has been a driving force, inspiring me to persevere and strive for excellence. Without her, this achievement would not be possible.

My sincere thanks go to Koç University Nanofabrication and Nanocharacterization Center for Scientific and Technological Advanced Research (N^2STAR) for providing the essential resources and a conducive environment for my research. I also would like to extend my appreciation to the administrative and technical staff at Koç University for their continuous support and for ensuring a smooth and productive research environment.

I want to express my deepest gratitude to my parents Meftun and İsmail Yener. I am grateful for their support and understanding throughout my life. I do not know how I could have achieved this without their support. I would like to specifically acknowledge my sister, Gözde Taşan, for her constant support, encouragement, and love. I feel like I am the luckiest brother on Earth. Thank you all for making this journey a memorable and rewarding experience.

Lastly, I would like to acknowledge the support of the National Scientific and Technological Council of Turkey (TÜBİTAK) for their financial assistance through the BIDEB 2210-A National Graduate Scholarship program, which made my research possible.

TABLE OF CONTENTS

LIST OF TABLES

LIST OF FIGURES

ABBREVIATIONS

AC	Alternating Current
BVD	Butterworth van-Dyke
EM	Electromagnetic
FFT	Fast Fourier Transform
IC	Integrated Circuit
KNN	Potassium Sodium Niobate
LIA	Lock-in Amplifier
LTRA	Lossy Transmission Line
OOK	On-Off Keying
PCB	Printed Circuit Board
PNIPAM	Poly(N-isopropylacrylamide)
PUC	Passive Ultrasonic Communication
PVA	Polyvinyl Alcohol
PZT	Lead Zirconate Titanate
SC	Short Circuit
SNR	Signal-to-Noise Ratio
SPICE	Simulation Program with Integrated Circuit Emphasis
US	Ultrasound

Chapter 1

INTRODUCTION

1.1 Piezoelectricity and Ultrasound

Piezoelectricity, which was discovered in 1881 [1], is the accumulation of electrical charges in a material in response to applied physical stress and the materials that show this phenomenon are called piezoelectric materials. In basic terms, mechanical and electrical domains in a piezoelectric material are coupled with each other. Materials undergo stress and strain when exposed to electrical field, and accumulate charge when exposed to stress [2].

Using the piezoelectric phenomenon, it is possible to vibrate a structure and disturb neighboring mediums such that acoustic waves are emitted. Therefore, piezoelectricity is the basis for most ultrasonic transducer[3]. Among various applications of ultrasonic transducers, medical ultrasound is the most popular field that use piezoelectricity to generate acoustic waves. Ultrasound probes excite piezoelectric elements with AC voltage and the generated acoustic (ultrasound) waves travel through the soft tissues and reflect when it reaches a boundary[4]. The reflected signals get detected by the same piezoelectric elements which convert acoustic pressures to electrical signals. The converted electrical signals form the basis of ultrasound images.

1.2 Wireless Communication Methods for Implantable Devices

Monitoring vital signs in deep tissues is a major challenge. Many diseases and disorders such as renal disorders, reproductive system disorders, and graft monitoring occur deep within the tissue, which limits the effectiveness of the measurement techniques that rely on superficial signs [5, 6, 7].

Medical imaging techniques such as ultrasonography and magnetic resonance imaging are helpful in getting clinically relevant information from deep tissues non-invasively, but they are not suitable for some cases where in-situ monitoring is necessary [8, 9]. For cases where superficial monitoring techniques and non-invasive imaging methods are not sufficient, it is possible to monitor signs deep within the body using invasive instruments like catheters [10, 11, 12]. Nonetheless, these alternatives are restricted to clinical settings, require trained personnel, and are costly for the healthcare system. Moreover, the invasive nature of these techniques holds the risk of causing severe discomfort, bleeding, scarring, and bacterial infections; thus, preventing frequent and continuous monitoring [13, 14, 15, 16, 17]. Therefore, monitoring vital signs deep within the body via wireless implants has been considered as an attractive solution.

As an alternative to the clinically available invasive measurement techniques, medical implants have demonstrated the ability to sense signals subcutaneously. Unlike early examples that used percutaneous wired connections to external devices, recent implantable devices used wireless power and data-transferring technologies such as inductive coupling[18, 19, 20, 21], magnetic resonance coupling[22, 23, 24], near-field communication[25, 26, 27], and Bluetooth[28, 29, 30].

Although various EM-based wireless data and power-transferring methods have been widely utilized in the literature, high tissue attenuation and low penetration depth associated with electromagnetic waves[31] either limited the implantation depth for these devices (Figure 1.1a); or necessitated wired connections between the deeply implanted sensor and subcutaneously implanted antenna (Figure 1.1b), which introduced similar risks associated with wired connections[32, 33].

1.3 Ultrasonic Communication Links

Power and data transferring via ultrasound (US) have recently attracted significant attention for deep-tissue implantable devices. US offers millimeter (below 1.5 MHz) and sub-millimeter (above 1.5 MHz) wavelengths at the diagnostic US frequency range, which achieves better coupling with miniaturized implants when compared to electromagnetic (EM) waves (wavelength of 25 mm at 2 GHz). Additionally, US offers

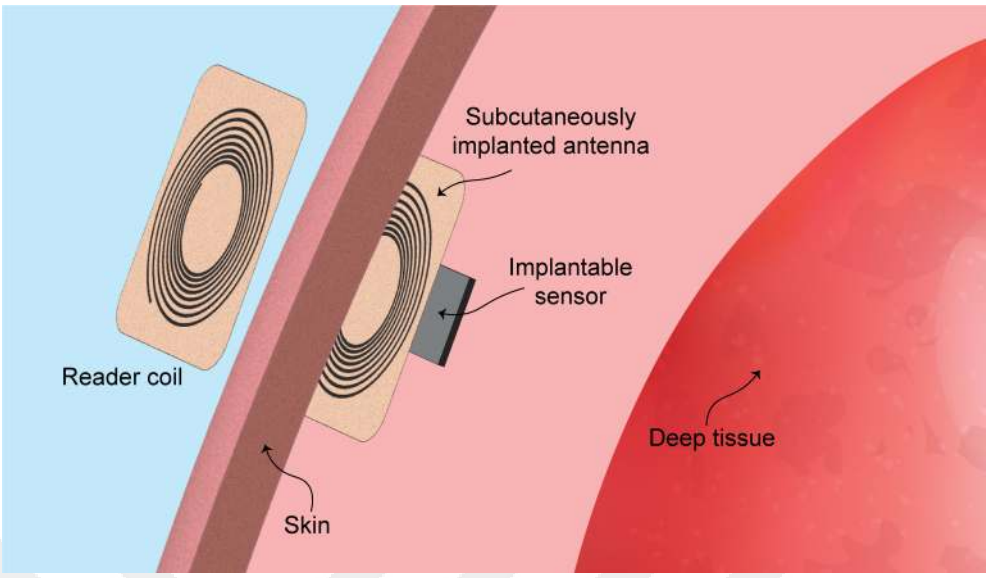

(a)

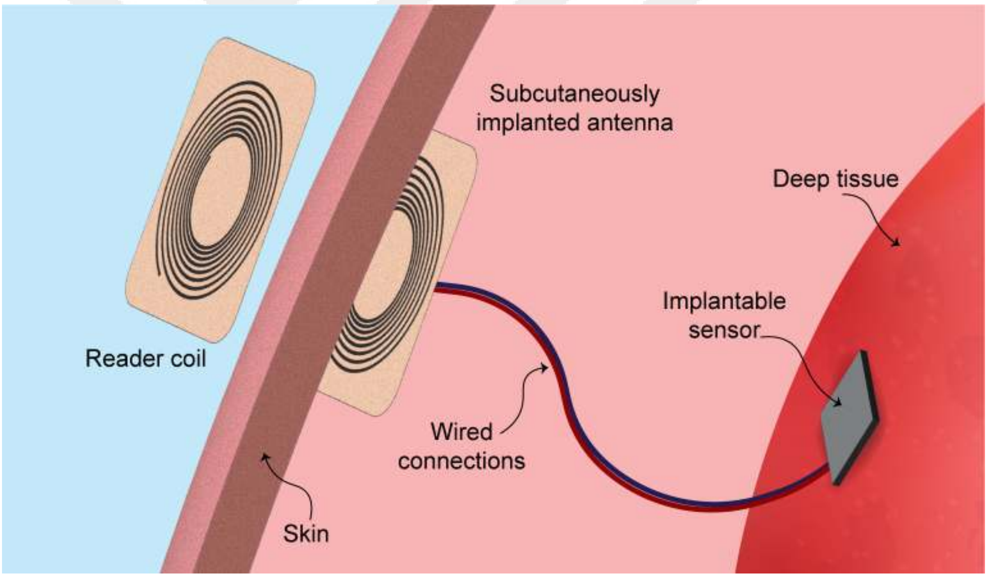

(b)

Figure 1.1: Most common wireless communication schemes using electromagnetic waves. (a) shows a subcutaneously implanted antenna and device, and (b) shows a deeply implanted sensor and subcutaneously implanted antenna with a wired connection in between.

lower attenuation in soft tissues which results in higher penetration depth and less tissue heating [31]. For these reasons, several studies demonstrated implantable devices with US power and data links [34, 35, 36, 37, 38, 39, 40, 41, 42] for various applications including wireless recording of the nervous system, and real-time tissue oxygenation and temperature monitoring. For instance, Sonmezoglu et al. developed a real-time tissue oxygenation monitoring device consisting of a luminescence sensor, an integrated circuit and a piezocrystal[39]. The custom integrated circuit is responsible for the power harvesting and data transfer. The system uses on-off keying (OOK) digital amplitude modulation technique to communicate. Based on the OOK sequence, the IC controls the modulation switch, which changes the resistive load connected to the piezocrystal and hence the amplitude of the ultrasound wave reflected from the piezocrystal. Similar to Seonmezoglu et al.'s study, all devices with modulation-based US data links demonstrated thus far need electronic components for power harvesting and active digital communication. As a result, these devices consist of capacitor elements to store energy, rectifier circuits to harvest power, and custom integrated circuit (IC) chips to modulate sensor data to the backscattered ultrasound waves and to switch between powering and data transferring modes, which leads to heavily customized and complex implant electronics design and fabrication. Alternatively, several studies have demonstrated electronics-free ultrasonic communication using implanted metamaterials [43, 44, 45, 46]. In a recent study, Tang et al. demonstrated metagels with special compositions for intracranial pressure, temperature and pH monitoring[46]. Each metagel composition deforms in response to a physical change in the environment (e.g. PVA/PNIPAM hydrogel for temperature sensing) and this changes the separation between the air fillers embedded inside the material. The change in the air filler separation causes the frequency of the incident ultrasound wave to shift as it reflects. In short, the main effect that facilitates wireless monitoring is the material composition. Therefore, these devices cannot be used for general-purpose communication methods as they rely on application-specific property changes of the metamaterials. Furthermore, a recent study demonstrated a passive ultrasound pressure sensing device leveraging the amplitude changes in impedance [47]. The acoustic coupling between the external and implanted piezocrystals caused electrical coupling thanks to the acoustic waves reverberating between the piezocrystals during the impedance measurements. Hence, the impedance amplitude of the implanted antenna effected by the connected capacitive load can be extracted from the external piezocrystal's impedance profile. Another study used the amplitude of the ultrasound pulse-echo signal as a wireless communication method[48]. In this study, a graphene solution-gated field-effect transistor is directly connected to a piezocrystal. Based on the voltage applied on the transistor gate, the resistance connected to the piezo changes which affects the amplitude of the reflected ultrasound wave. Although these solutions are truly electronics-free, amplitude-based approaches have limited applicability as they are highly susceptible to disturbances in the acoustic coupling.

1.4 Motivation and Objectives

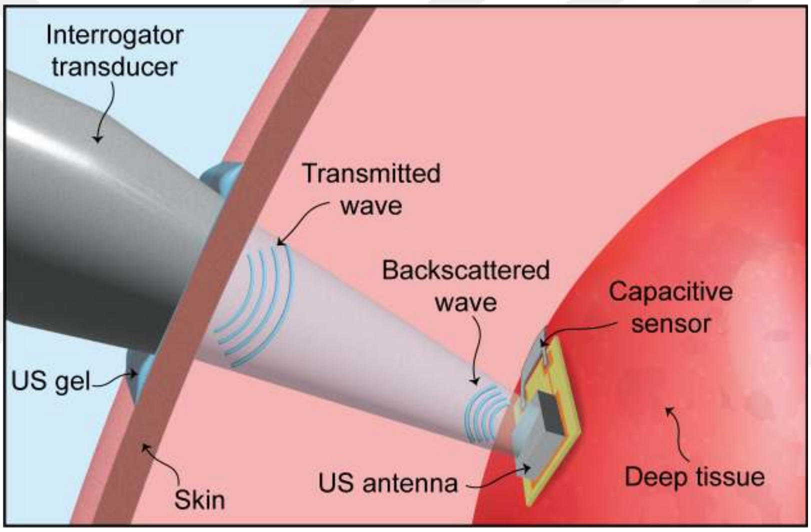

Figure 1.2: Working principle of the proposed ultrasonic communication scheme. A capacitive sensor and an ultrasonic antenna consisting of a single PZT are illustrated on deep tissue. An external interrogator transducer transmits ultrasound waves toward the antenna and records the backscattered waves.

Considering the current literature and state-of-the-art, there is a pressing need to improve the wireless communication methods. Existing solutions were able to solve the problems regarding achieving efficient coupling between the implanted antenna and the external device. However, the use of modulation not only necessitated integrated circuits which increased the level of customization and complexity but also moved implants away from passive operation because additional power harvesting or storing elements have to be introduced in order to power the implanted electronics. Therefore, one can explore the passive operation for ultrasound links similar to inductive coupling.

The objective of this thesis is to propose and demonstrate a wireless passive, and hence electronics-free, ultrasonic communication method. Figure 1.2 depicts the scheme this thesis aims to achieve. A simple ultrasonic antenna consisting of only a single piezoelectric element (used as an ultrasonic antenna) and a substrate for electrical connections, which establishes a universal antenna scheme that can be used for any implantable capacitive sensor, similar to the ones used for inductive coupling method.

1.5 Thesis Organization

Including the introduction chapter, this thesis is presented in 5 chapters[1]. The organization of the manuscript is as follows:

Chapter 1: Introduction chapter covers the basics regarding piezoelectricity and ultrasound. Additionally, electromagnetic wave-based wireless communication literature is discussed with an emphasis on implantable applications. Recent developments in ultrasound linkages for wireless data and power transfer are explained with their advantages and shortcomings. Finally, the motivation and research objectives of this thesis are presented.

Chapter 2: In this chapter, we showcase the working principle of the proposed technology with the help of mathematical modeling. First, capacitive loads and their effects on the resonance characteristics of a piezoelectric element are analyzed, followed by the discussion about the resistive load effect. The findings of this chapter form the building block of the research objective of this thesis.

Chapter 3: In this chapter, we discuss the details regarding the design, fabrication and characterization of the fabricated ultrasonic antenna. The design criteria and fabrication flow are explained, and a fabricated ultrasonic antenna is characterized electrically and acoustically.

Chapter 4: This chapter is dedicated to the in vitro demonstration of the proposed passive ultrasonic communication (PUC) method. The in vitro experiment setup and its components are explained, and the experiment results are presented.

Chapter 5: In this chapter, the advantages and drawbacks of the PUC method are

[1]This thesis is based on a recently submitted research article by the author.

discussed. The promising findings are presented and possible solutions for the drawbacks are mentioned.

Chapter 2

WORKING PRINCIPLE AND MATHEMATICAL MODELING

Establishing a passive ultrasonic communication necessitates property or characteristic changes naturally occurring in the implanted device. Therefore, active components such as integrated circuits (ICs) cannot be used.

The most common way of exploiting property changes in piezoelectric materials is to study the resonance characteristics of the material. To this end, the effects of capacitive and resistive -the most common passive sensor types used for implantable applications- loads on the resonance behavior of the US antenna were analyzed in this chapter.

2.1 Capacitive Load Effect

An equivalent circuit is the representation of a system based on electric network theory. The parts of a complex physical system can be lumped and treated as individual components in an electrical circuit, which result in an accurate and computationally lightweight simulations. Therefore, lumped modeling was chosen to analyze the effect of capacitive load. In particular, Butterworth-van-Dyke (BVD) model was used to analyze the resonance characteristics of a piezoelectric crystal, while Leach model was used to simulate the system including the acoustic domains.

2.1.1 Butterworth Van-Dyke Model

Understanding the frequency characteristics of a piezoelectric crystal is crucial for the proposed passive communication method and the BVD equivalent circuit model has been recognized by many researchers and it is also recommended by the IEEE Standard on Piezoelectricity [49, 50]. Therefore, the resonance and anti-resonance characteristics of the antenna and how it reacts to capacitive loads are analyzed in this section.

In Figure 2.1a, the BVD circuit of a piezoelectric material is shown. The circuit

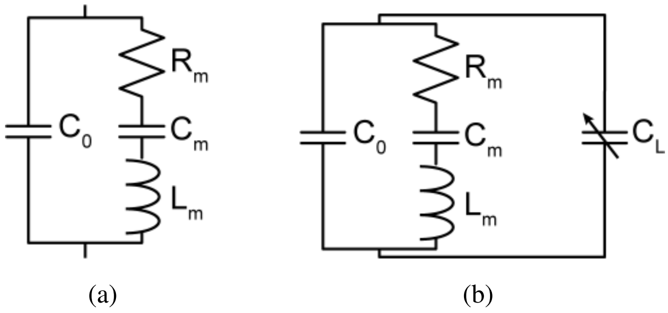

Figure 2.1: Butterworth-van-Dyke circuits of the piezoelectric element with (a) and without (b) a capacitive load connected in parallel.

has two branches representing electrical and mechanical behavior. The capacitor (C_0) in the electrical branch represents the clamped capacitance (nominal capacitance), whereas the resistor (R_m), capacitor (C_m), and inductor (L_m) in the mechanical branch represent damping, elastic compliance, and equivalent mass, respectively.

The resonance frequency (series resonance) of a circuit is at which the impedance is minimum. In contrast, the anti-resonance (parallel resonance) frequency occurs when the impedance of the circuit is maximum. The complex impedance of the BVD model can be written as [51]:

$$Z = \frac{\left(R_m + j\omega L_m + \dfrac{1}{j\omega C_m}\right)\dfrac{1}{j\omega C_0}}{R_m + j\omega L_m + \dfrac{1}{j\omega C_m} + \dfrac{1}{j\omega C_0}} = \frac{R_m + j\left(\omega L_m - \dfrac{1}{\omega C_m}\right)}{1 + \dfrac{C_0}{C_m} - \omega^2 L_m C_0 + j\omega R_m C_0} \tag{2.1}$$

The series resonance frequency can be computed by making the imaginary part of the numerator zero, while the parallel resonance frequency can be computed by making and parallel resonance frequencies can be found by making the real part of the denominator zero[52, 53, 54]. Hence, resonance frequencies can be written as:

$$f_s = \frac{1}{2\pi\sqrt{L_m C_m}} \tag{2.2}$$

$$f_p = \frac{1}{2\pi\sqrt{L_m \dfrac{C_m C_0}{C_m + C_0}}} \tag{2.3}$$

With the load capacitance added to the circuit (as shown in Figure 2.1b), the electrical branch can be simplified. The total effective capacitance at the electrical branch can be written as:

$$C_T = C_0 + C_L \tag{2.4}$$

Connecting the load capacitance to the BVD model in parallel, the new (parallel) anti-resonance frequency can be written as:

$$f_{pL} = \frac{1}{2\pi\sqrt{L_m \frac{C_m C_T}{C_m + C_T}}} \tag{2.5}$$

As a result, connecting a capacitor element in parallel to the BVD circuit changes the parallel resonance frequency of the transducer but the series resonance does not get affected as evident from Equation 2.2.

Equation 2.5 suggests an inverse relationship between the anti-resonance frequency and the load capacitance. For instance, when the load capacitance increases, the new anti-resonance frequency, f_{pL}, decreases [55].

The parameters of the new anti-resonance frequency are,

$$C_0 = A\varepsilon_{33}^T / t \tag{2.6}$$

$$C_m = \frac{8C_0 k_{eff}^2}{\pi^2 - 8k_{eff}^2} \tag{2.7}$$

$$L_m = \frac{1}{4\pi^2 f_{sc}^2 C_m} \tag{2.8}$$

$$R_m = \frac{1}{8k_{eff}^2 f_{sc} C_0} \frac{Z_F + Z_B}{Z_C} \tag{2.9}$$

$$f_{oc} = \frac{v_p}{2t} \tag{2.10}$$

$$f_{sc} = \left(1 + \frac{8}{\pi^2} \cdot \frac{k_{eff}^2}{1 - k_{eff}^2}\right)^{-1/2} f_{oc} \tag{2.11}$$

where A, t, e_{33}^T, v_p, k_{eff} are area, thickness, dielectric constant of the piezoelectric element, the speed of sound, and electromechanical coupling coefficient, respectively. Z_F, Z_B, and Z_C are the products of respective acoustic impedances and areas for front and back ports and the transducer, respectively. And finally, f_{oc} and f_{sc} are the open- and short-circuit frequencies, respectively.

Table 2.1: Butterworth van-Dyke parameters.

Parameters	**Values**	**Parameters**	**Values**
Thickness, t $[m]$	0.001	Relative Dielectric, ε_{33}^{T}	3400
Speed of Sound, v_p $[m/s]$	3850	Electromechanical Coupling Coefficient, k_{eff}	0.75
Front Port Specific Acoustic Impedance, Z_B $[MRayl]$	1.50	Back Port Specific Acoustic Impedance, Z_B $[MRayl]$	4.3910^{-4}
Transducer Specific Acoustic Impedance, Z_C $[MRayl]$	28.9	Load Capacitance, C_L $[pF]$	$[0, 400]$

A representative study was conducted to observe new anti-resonance frequency as the load capacitance changes. Using Equation 2.5 and parameters in Table 2.1, the shifts in anti-resonance frequency are plotted for varying surface area, hence varying nominal capacitance.

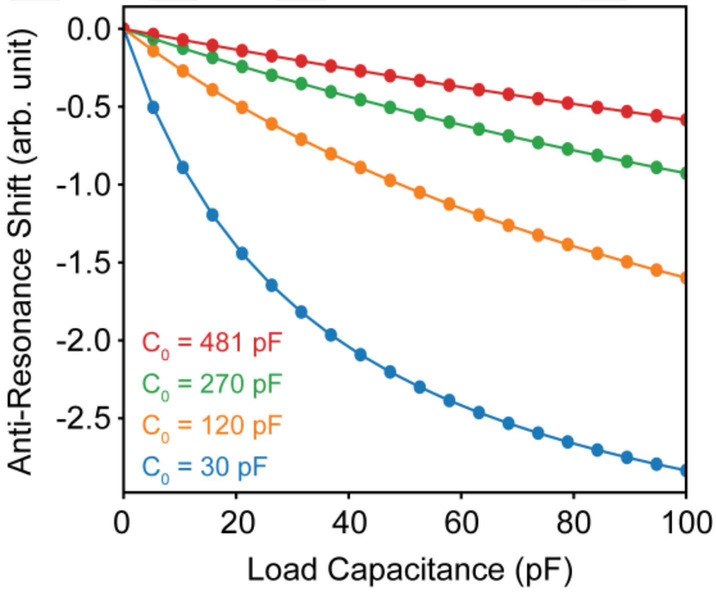

Figure 2.2: Representative anti-resonance shift comparison plot for various nominal piezoelectric element capacitance.

Figure 2.2 shows anti-resonance shift curves for four different piezoelectric nominal capacitance values. Specifically, the curves correspond to 1x1, 2x2, 3x3, and 4x4 mm^2

piezoelectric surface areas. The results show that the nominal capacitance of the piezoceramic has a strong influence in the slope of the anti-resonance shift.

2.1.2 Leach Model

Acoustic systems can be represented by various models. Popular equivalent circuit models for acoustic systems are KLM, Mason, Redwood, and Leach. The Mason model features elements with negative capacitance [56], which is challenging to model in SPICE software. The KLM and Redwood models, on the other hand, eliminate the presence of negative capacitance by incorporating transformer elements into the equivalent circuit models, which are frequency-dependent [57, 58]. In contrast, the Leach electroacoustic analogous circuit does not need any negative capacitance and uses controlled sources instead of relying on frequency-dependent transformers for the electromechanical coupling [59]. Therefore, the Leach model was selected for the mathematical modeling due to its SPICE-friendly nature.

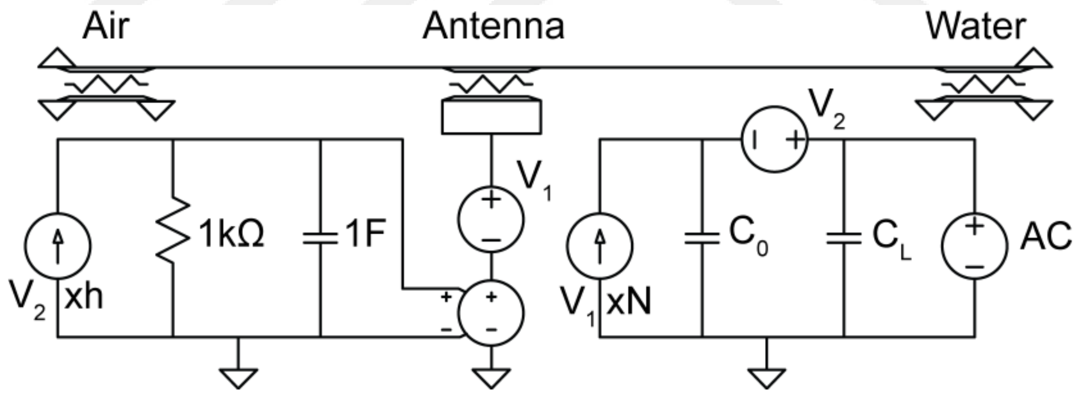

Figure 2.3: Leach analogous electromechanical model of the system.

Figure 2.3 shows the Leach model constructed in LTspice software. Material specific parameters (N, h, and C_0) were calculated using the below formulae.

$$h = \varepsilon_{33} \cdot e^{S} \tag{2.12}$$

$$C_0 = e^{S} \cdot \frac{A}{l} \tag{2.13}$$

where ε_{33}, e^S, A and l are short circuit elastic constant, clamped dielectric constant, surface area and thickness of the piezoelectric element, respectively. Then, parameter N can be calculated using Equations 2.12 and 2.13.

$$N = h \cdot C_0 \tag{2.14}$$

Based on the material properties of the PZT-5H piezoceramic (Navy VI, APC International Ltd.), the N, h and, C_0 parameters were calculated as shown in Table 2.2.

Table 2.2: Leach model parameters.

Parameters	N	h	C_0 [pF]
Values	0.1764	$0.671 \cdot 10^9$	262.96

The ultrasonic transducer as well as the back and front acoustic ports were modeled as lossy transmission lines. The capacitor element named C_L represents the capacitive load connected to the transducer in parallel. The lossy transmission line parameters were calculated using the below formulae. The thicknesses of the air and water mediums were selected as high as 1000 m so that there would be no echo signals disturbing the steady-state analysis.

$$L_{ltra} = \rho \cdot A \tag{2.15}$$

$$C_{ltra} = \frac{1}{v^2 \cdot L_{ltra}} \tag{2.16}$$

$$R_{ltra} = 2\pi \cdot f_0 \cdot L_{ltra} \cdot Q \tag{2.17}$$

where ρ, v, and Q are the density of the material, and speed of sound in transducer, and quality factor of the material, respectively. f_0 is the center frequency of the transducer, which can be calculated using $f_0 = v/l$, where v and l are the speed of sound and the thickness.

Although Equation 2.17 is a suitable formula for piezoelectric elements, center frequency, and quality factor are not meaningful parameters for acoustic mediums like air and water. Therefore, an alternative equation can be used for those mediums to calculate the resistance of their representative lossy transmission line.

$$R_{ltra,2} = 2\rho \cdot v \cdot A \cdot \alpha \tag{2.18}$$

where α is the attenuation coefficient of the acoustic medium. The LTRA parameters for the air, piezoelectric element (antenna), and water are presented in Table 2.3.

Table 2.3: Lossy Transmission line (LTRA) parameters.

LTRA	$R\ [\Omega]$	$L\ [H]$	$C\ [F]$	$l\ [m]$
Air	19.159	$1.164 \cdot 10^{-5}$	0.730	1000
Antenna	$14.863 \cdot 10^{3}$	0.068	$7.232 \cdot 10^{-7}$	0.001
Water	11.856	0.009	$4.948 \cdot 10^{-5}$	1000

The equivalent model was simulated under stead-state conditions between 1.5- and 2.5-MHz frequencies, while the load capacitance (C_L) was kept at zero (Figure 2.4).

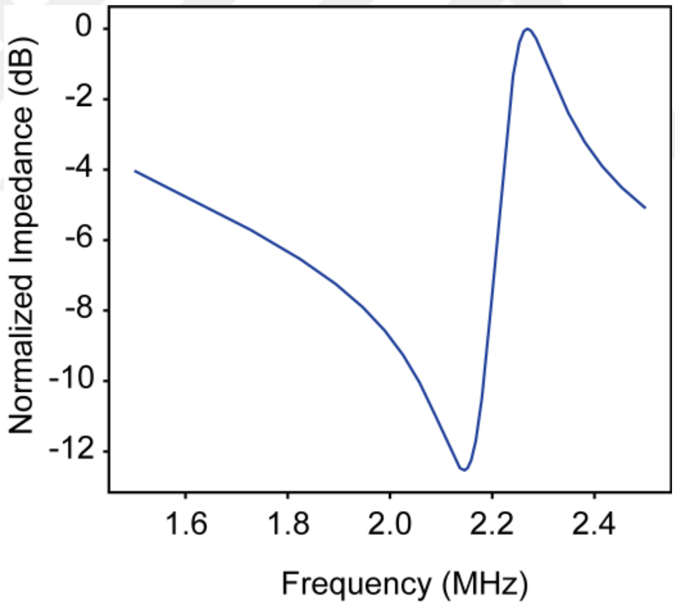

Figure 2.4: LTspice Steady-state AC simulation results showing the normalized absolute impedance curve of the transducer.

The simulation results show resonance and anti-resonance frequencies at 2.14- and 2.27-MHz, respectively. The lumped simulation was repeated for load capacitance values between 0 and 110 pF and the results (presented in Figure 2.5) clearly show that the anti-resonance frequency of the antenna decreases as the load capacitance value increases.

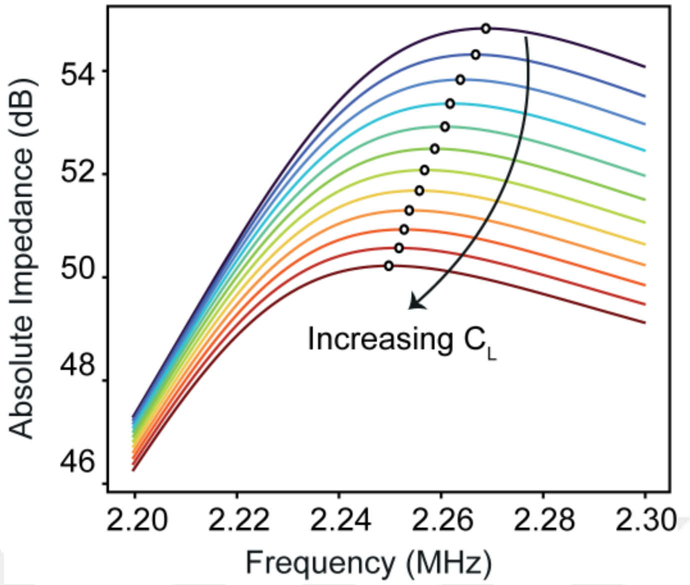

Figure 2.5: LTspice simulation results showing the absolute impedance of the transducer with various capacitive loads connected in parallel.

2.2 Resistive Load Effect

The complex impedance matrix of a 3-port (electrical, acoustic front and back) transducer connected to an electrical load can be written as[60, 61],

$$Z = \begin{bmatrix} Z_{11} & Z_{12} & Z_{13} \\ Z_{12} & Z_{22} & Z_{13} \\ Z_{13} & Z_{13} & Z_{33} \end{bmatrix} = -j \cdot \begin{bmatrix} Z_p \cot(k_p t_p) & Z_p \csc(k_p t_p) & h_{33}/\omega \\ Z_p \csc(k_p t_p) & Z_p \cot(k_p t_p & h_{33}/\omega) \\ h_{33}/\omega & h_{33}/\omega & 1/(\omega C_p) \end{bmatrix} \tag{2.19}$$

where $Z_p = \rho_p c_p A_p$ is the mechanical impedance of the transducer (ρ_p, c_p, and A_p are the density, speed of sound and area, respectively.), ω is the angular frequency, t_p is the thickness, $k_p = \omega/c_p$ is the wavenumber in the transducer, $C_p = \varepsilon_{33}^S A_p/t_p$ is the nominal capacitance where ε_{33}^S is the clamped permittivity, and $h = e_{33}/\varepsilon_{33}^S$ is the transmitting coefficient where e_{33} is the clamped piezoelectric voltage constant.

The input mechanical impedance (Z_{in}) of the piezoelectric block, poled in its thickness direction, can be written as:

$$Z_{in} = Z_{11} - \frac{Z_{12}^2 - \dfrac{Z_{12}Z_{13}^2}{Z_e + Z_{33}}}{Z_b + Z_{11} - \dfrac{Z_{13}^2}{Z_e + Z_{33}}} - \frac{Z_{13}^2 - \dfrac{Z_{12}Z_{13}^2}{Z_b + Z_{11}}}{Z_e + Z_{11} - \dfrac{Z_{13}^2}{Z_b + Z_{11}}} \tag{2.20}$$

where Z_e and Z_b, are complex impedance of the electrical load connected to the piezoceramic block and the backing layer impedance, respectively.

The acoustic reflection coefficient can be written as shown below [60], where Z_w is the characteristic acoustic impedance of water.

$$S_{11} = \frac{Z_w - Z_{in}}{Z_w + Z_{in}} \tag{2.21}$$

Equation 2.21 was numerically solved for a 3x3x1 mm^3 PZT-5H transducer using a Python script. The electrical load connected to the transducer (Z_e) was varied from 0Ω (Short-circuit condition) to $100k\Omega$. The results are presented in Figure 2.6), which reveal an acoustic reflection behavior depending on the electrical load impedance connected to the piezoelectric block. Assuming that the PZT block has a (series) resonance impedance of Z_r and an anti-resonance (parallel resonance) impedance of Z_p. Characteristically, Z_p is greater than Z_r. For electrical loads with impedance greater than Z_p (for $Z_e \geq Z_p$), the lowest acoustic reflection occurs at the anti-resonance frequency. As the electrical load drops from Z_p to Z_r (for $Z_r < Z_e < Z_p$), the minimum acoustic reflection frequency shifts from the anti-resonance frequency of the transducer to the resonance frequency. Similarly, when the electrical impedance load is less than or equal to Z_r (for $Z_e \leq Z_r$), the lowest acoustic reflection occurs at the resonance frequency of the transducer (Figure 2.6).

2.3 Working Principle

The behavior observed for the resistive load can be leveraged in conjunction with the capacitive effects discussed in Section 2.1. While the electrical impedance of the capacitive sensor is above Z_p, the capacitance of the sensor shifts the anti-resonance frequency at which the lowest acoustic reflection occurs. Moreover, as the sensor capacitance increases, and its impedance moves in between Z_p and Z_r, the frequency of the lowest acoustic reflection shifts. Therefore, this minimum acoustic reflection

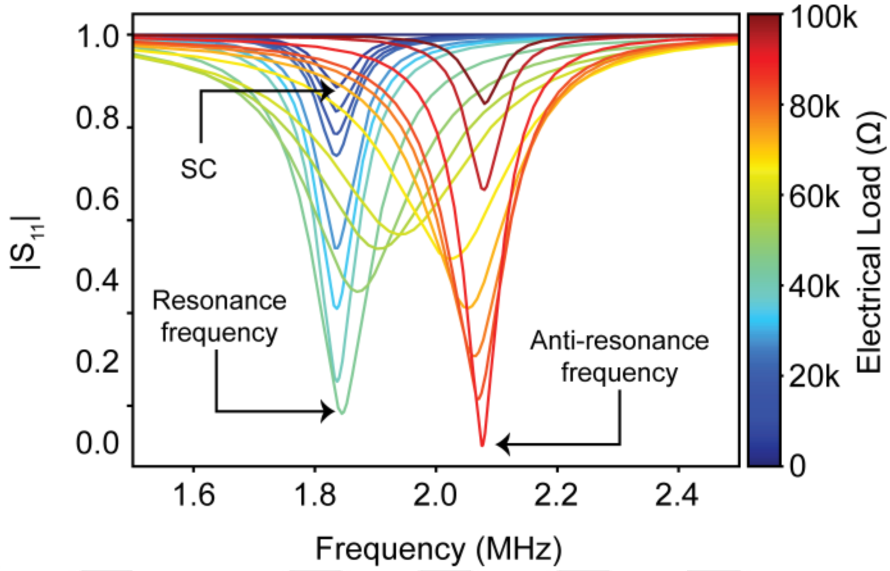

Figure 2.6: Acoustic reflection coefficient spectrum. Generated by a Python script using PZT-5H material properties.

frequency can be captured by an external interrogator transducer, and enable wireless data transfer between the deeply implanted sensor and an external ultrasound probe (Figure 2.7).

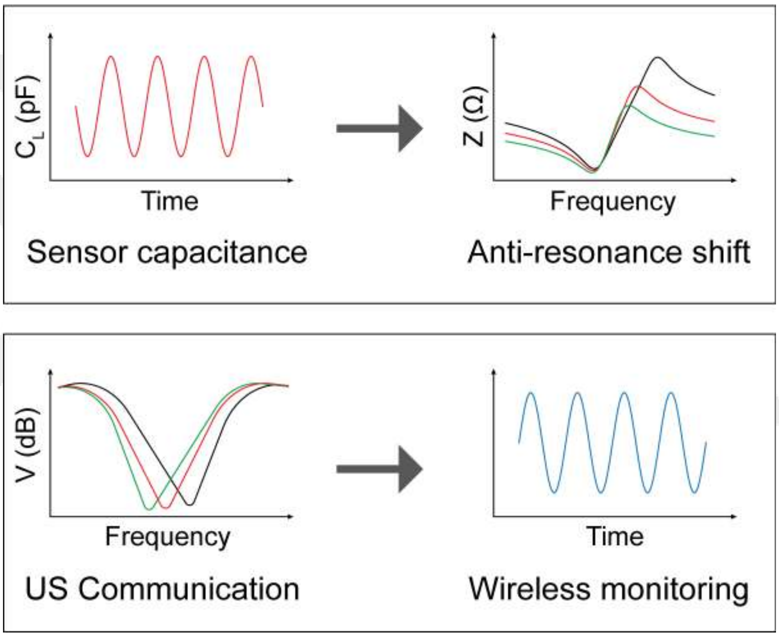

Figure 2.7: The proposed working principle of the wireless and electronics-free ultrasonic communication method. Sensor capacitance causes shifts in the anti-resonance frequency of the US antenna. The shifted anti-resonance frequency gets detected by the wireless PUC method, which enables wireless monitoring of vital signs in deep tissues.

Chapter 3

ANTENNA DESIGN, FABRICATION AND CHARACTERIZATION

3.1 Design of the Ultrasonic Antenna

The ultrasonic antenna consists of a single piezoelectric element soldered on a substrate. ML-104 printed circuit board was selected for the substrate due to its thin (200 μm) profile, reducing the overall thickness of the device.

As can be seen from Section 2.1.1 the nominal capacitance of the antenna is crucial for the sensitivity of the system. The lower the nominal capacitance of the piezoelectric element, the higher shifts are observed. Therefore, it is crucial to select the material and dimensions of the piezoelectric element and the capacitive range of the sensor simultaneously. PZT-5H was selected as the piezoelectric material due to its high dielectric constant[62]. Additionally, the capacitive pressure sensor used in this thesis during the in-vitro demonstration (Chapter 4) showed around 100 pF of capacitive change under medically relevant pressures[63, 64, 65, 66]. As a result, the dimensions of the US antenna were selected as 3x3x1 mm^3, which resulted in a nominal capacitance of approximately 250 pF, in order to achieve high sensitivity and linearity.

Conventional ultrasonic transducers use heavy and lossy materials as backing in order to dissipate the acoustic waves going towards the back side and to dampen the piezoelectric element to eliminate the ringdown effect, which increases the axial resolution of the transducer[67]. Furthermore, using a heavy backing material would result in a broader resonance profile with a lower quality factor. However, the US antenna presented in this thesis uses air as the backing material. Unlike conventional ultrasonic transducers, the task of the US antenna is not to perform imaging. Therefore, axial resolution was not a design criterion. Additionally, broadening the resonance profile would obstruct the goal of this study, since the PUC method relies on tracking the anti-resonance frequency of a piezoelectric element.

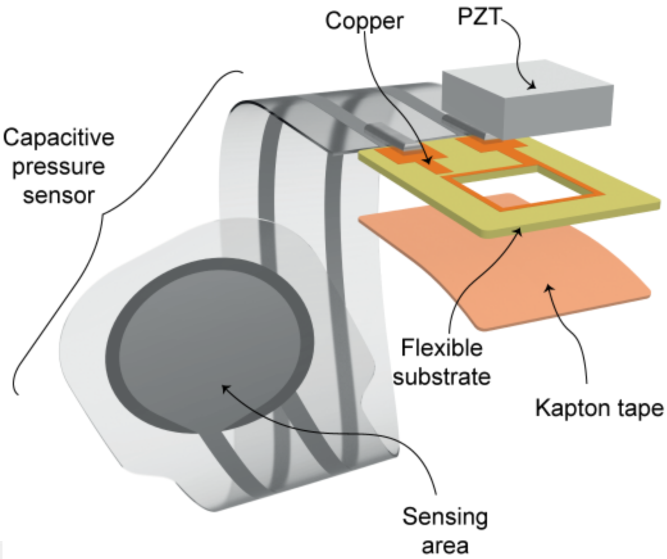

Figure 3.1: Exploded view of the ultrasonic antenna design.

In order to realize the air-backing design, a square-shape cut was created on the ML-104 printed circuit board (PCB). The Kapton tape placed on the bottom surface of the PCB seals the air gap created by the square-shaped cut. The exploded view of the US antenna design is presented in Figure 3.1.

3.2 Fabrication of the Ultrasonic Antenna

A 1 mm thick bulk PZT-5H plate was purchased from American Piezo (APC - 855). The fabrication of the US antenna started with the dicing of the bulk piezoceramic. using a wafer dicer (DAD3221, DISCO) to get 3x3x1 mm^3 pieces.

The R4 laser machining device (LPKF Laser & Electronics) was used to pattern the conductive traces on the flexible ML-104 PCB substrate and to cut a square shape where the piezoelectric element was to be placed.

After the dicing and laser patterning steps were completed, the piezoelectric crystal was soldered on the flexible PCB using a low-temperature solder (TS391LT, Chip Quik). First, the copper surfaces of the PCB were covered with solder. This process was done to avoid the oxidation of the conductive surfaces. Then, the piezoelectric element was placed on the PCB and the solder under the piezoelectric element was heated to the establish

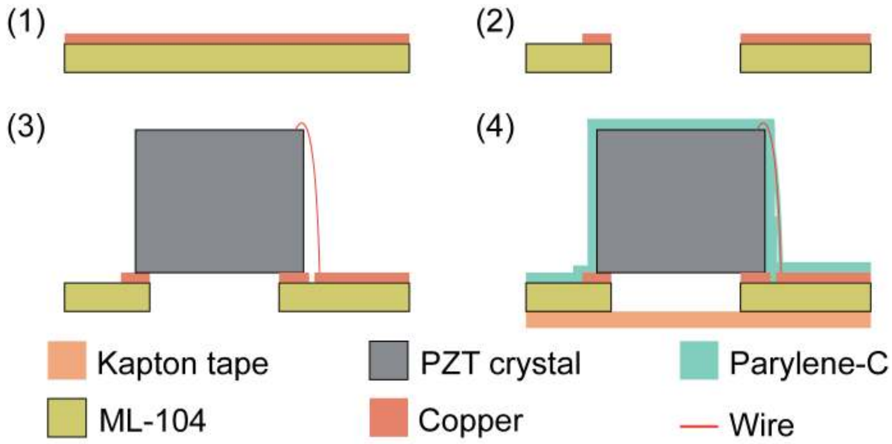

Figure 3.2: Fabrication flow of the ultrasonic antenna.

electrical connection for the bottom electrode of the PZT. The top electrode connection was established by manually soldering a thin copper wire between the PZT surface and a conductive trace on the PCB.

In order to seal the air cavity at the back of the PZT, a Kapton tape was placed on the bottom surface of the PCB. As a final step, the device was coated with a biocompatible Parylene-C using PPS Labcoater Series 100 in order to achieve electrical and chemical isolation. The schematic fabrication flow of the US antenna is presented in Figure 3.2.

Figure 3.3 shows the image of a fabricated US antenna with a 5x7 mm^2 footprint and a total volume of 16 mm^3.

3.3 Antenna Characterization

The fabricated ultrasonic antenna was electrically and acoustically characterized. The electrical characterization of the device was done using an impedance analyzer (MFIA, Zurich Instruments) in distilled water. The absolute impedance of the device are compared to the simulation results in Figure 3.4. As can be seen from the results, the resonance profile of the fabricated device does not match exactly with the simulation results. This is due to the fact that the selected dimensions for the piezoelectric element do not comply with the suggested aspect ratio rules. For thickness mode piezoceramics, an aspect ratio of 10 is recommended, which successfully isolates the thickness mode from other vibration

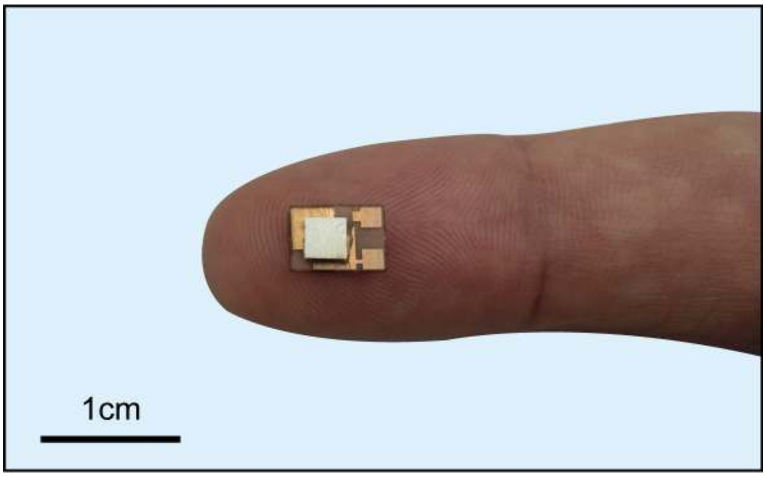

Figure 3.3: Optical image of the fabricated US antenna before its top electrode is soldered on the copper traces of the conductive substrate.

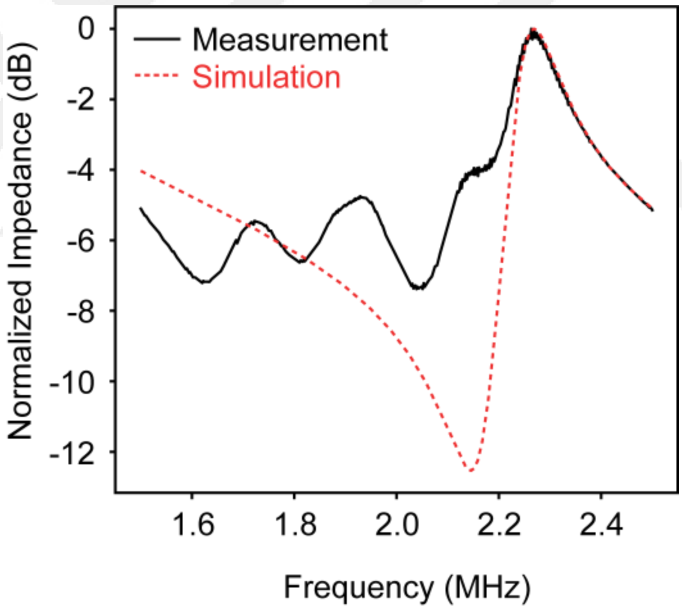

Figure 3.4: Absolute impedance measurement of the ultrasonic antenna compared to the LTspice simulation result.

modes[68]. Therefore, the vibration modes of a 3x3x1 mm^3 PZT element are not isolated, and multiple resonances can be observed around the expected resonance frequency of the antenna. The reason why measurement and simulation results do not match is the fact that the idealized Leach model does not account for the aspect ratio of the piezoelectric element and hence shows the thickness mode perfectly isolated.

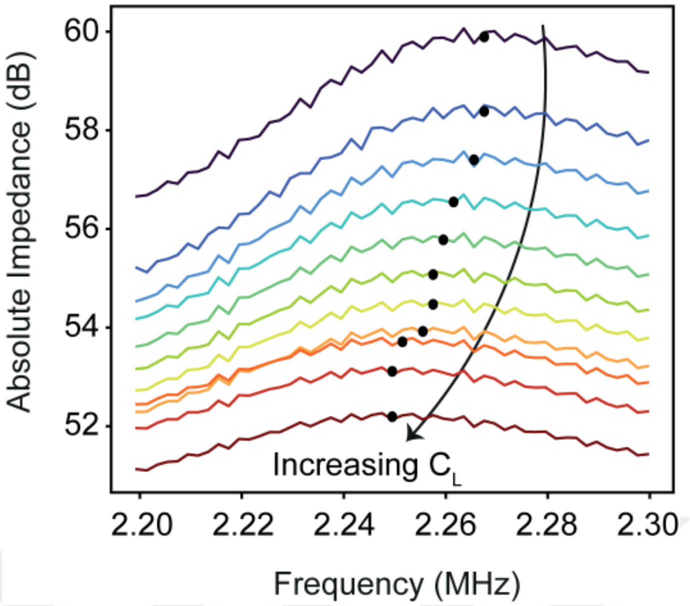

Figure 3.5: Absolute impedance measurements of the ultrasonic antenna with varying capacitive load connected in parallel.

The impedance measurements of the antenna were repeated for various capacitive loads. To this end, the US antenna was submerged in a distilled water tank and its electrodes were connected to a breadboard using copper wires. Then, a variable capacitor element and the impedance analyzer were connected to the breadboard. The resulting impedance profiles are displayed in Figure 3.5. The results clearly show that the anti-resonance frequency of the antenna shifts as the capacitive load connected in parallel changes. The noise observed in the measured impedance profile was due to uncontrolled echo signals disturbing the steady-state measurements.

The anti-resonance peaks of the absolute impedance profiles were extracted from the measurement and simulation data using a Python script. The resulting scatter plot is shown in Figure 3.6.

Since the antenna vibrates during passive communication, it emits and reflects ultrasound waves. Therefore, two acoustic characterization tests were performed using a 0.5-mm diameter needle hydrophone (Precision Acoustics). The frequency sweep experiment was conducted to observe the acoustic pressure amplitudes generated by the antenna at various frequencies. An arbitrary waveform generator (33521B Waveform

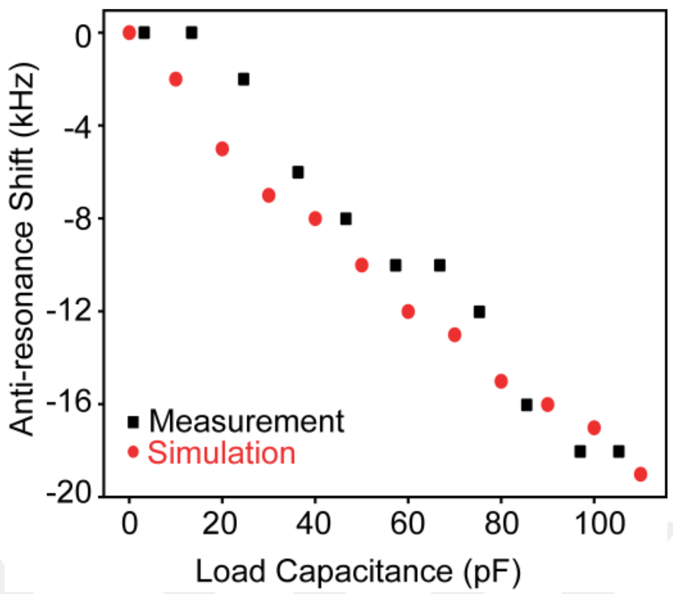

Figure 3.6: Anti-resonance peak shift comparison of the measured and simulated impedance profiles.

Generator, Keysight) was connected to the antenna while the hydrophone was connected to an oscilloscope. The ultrasonic measurement system (UMS-Research, Precision Acoustics) was used to automatically sweep the frequency of interval. The test results showed that the maximum acoustic pressure was generated at 2.02-MHz, which supports the claim that the antenna is working at its thickness mode. Furthermore, the acoustic pressure profile was acquired using the same UMS-Research setup. The hydrophone was mounted on the motorized stage and the pressure profile was measured at a 25x25 grid with 0.4 mm increments. The acquired 25x25 pressure matrix was interpolated to a 250x250 matrix to increase the resolution. Figure 3.7 shows the acoustic characterization test results.

3.4 Communication Link Characterization

The proposed passive ultrasonic communication link was established between a commercial immersion transducer (V323-SU, Olympus) and a 3x3x1 mm^3 fabricated ultrasonic antenna. The schematic block diagram of the hardware system is displayed in Figure 3.8. The experiment was conducted in distilled water. The load capacitance was

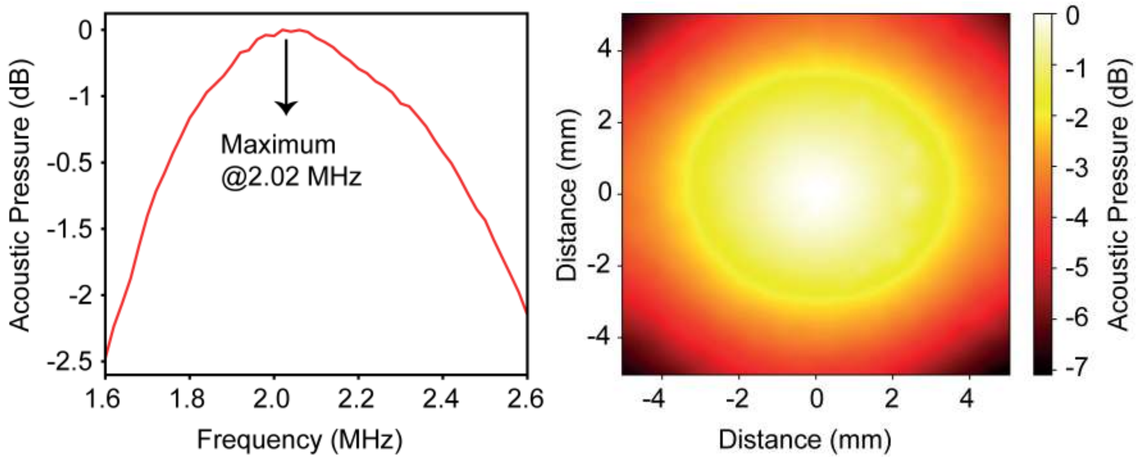

(a) (b)

Figure 3.7: Acoustic characterization results. (a) Frequency sweep test result showing the maximum acoustic pressure for a range of frequencies. (b) Acoustic pressure profile of the antenna, revealing a 9.4 mm -3dB diameter 3 cm away from the source.

varied using a variable capacitor (PPZN60100, Passive Plus). The excitation and signal processing operations were performed by a lock-in amplifier (LIA) device (UHFLI, Zurich Instruments). A duplexer (RDX-6, RITEC Inc.) was used to enable transmit and receive operations from the same interrogator transducer.

The internal oscillator of the lock-in amplifier device determines the frequency of the generated excitation signals which are then amplified by an RF amplifier (F30PV, Pendulum). The echo signals received by the LIA are mixed with a sinusoidal waveform at the same frequency as the excitation signal and demodulated with a low-pass filter, which forms the envelope of the unprocessed time-domain signal.

Figure 3.9a shows a raw pulse-echo waveform at exactly 2 MHz whereas the demodulated form of the echo signal is shown in Figure 3.9b. After the signal is demodulated, the lock-in amplifier calculates the average signal level within the demodulator trigger interval. These pulse-echo measurements are repeated for every frequency until the entire frequency interval is swept. The minimum point (valley) in the resulting frequency-dependent amplitude spectrum corresponds to the frequency of the lowest acoustic reflection.

Figure 3.10 shows a communication sweep and time-domain pulse-echo waveforms

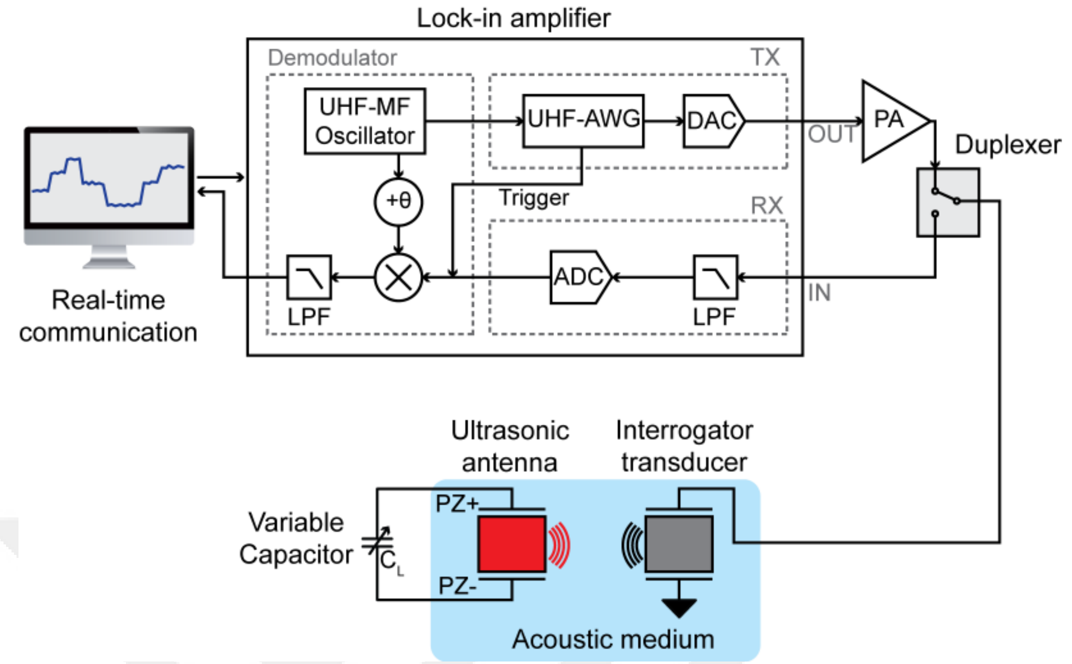

Figure 3.8: Hardware block diagram of the ultrasonic communication system setup.

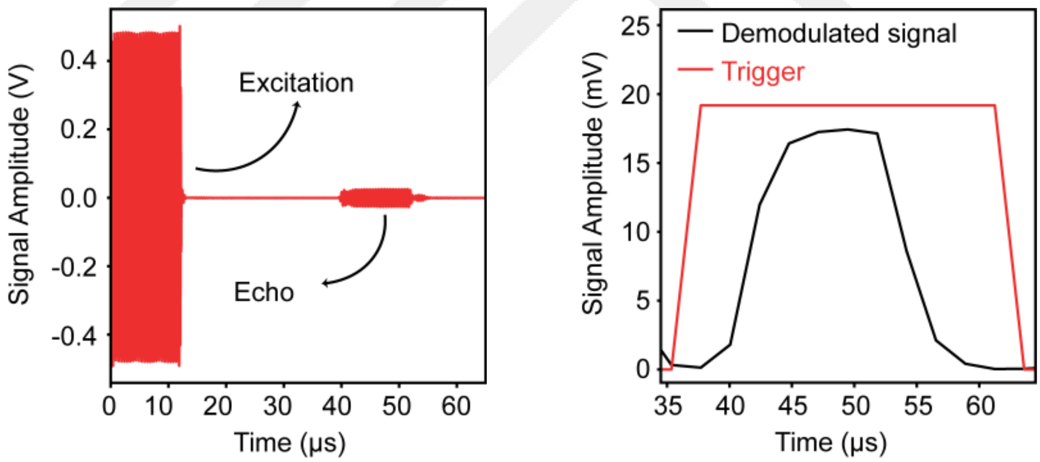

(a) (b)

Figure 3.9: Backscattered signal processing. (a) Time domain waveform of the pulse echo signal before any signal processing. (b) The demodulated backscatter signal and demodulator trigger signal.

captured at two different frequencies. The communication sweep (Figure 3.10a) reveals the frequency of the lowest acoustic reflection as 2.281 MHz. As described in Section 2.2, the amplitude of the backscattered signal is expected to be the lowest at this frequency. Figures 3.10b and 3.10c show pulse-echo waveforms captured at 2.2- and 2.281-MHz frequencies, respectively. The plots clearly show that the amplitude of the backscattered signal is less for the 2.281-MHz waveform. This frequency-dependent behavior creates the shape of the communication sweep spectrum.

In terms of signal quality, a 2-MHz $30V_{pp}$ excitation signal results in an echo signal-to-noise ratio (SNR) of approximately 1072 at a depth of 3 cm.

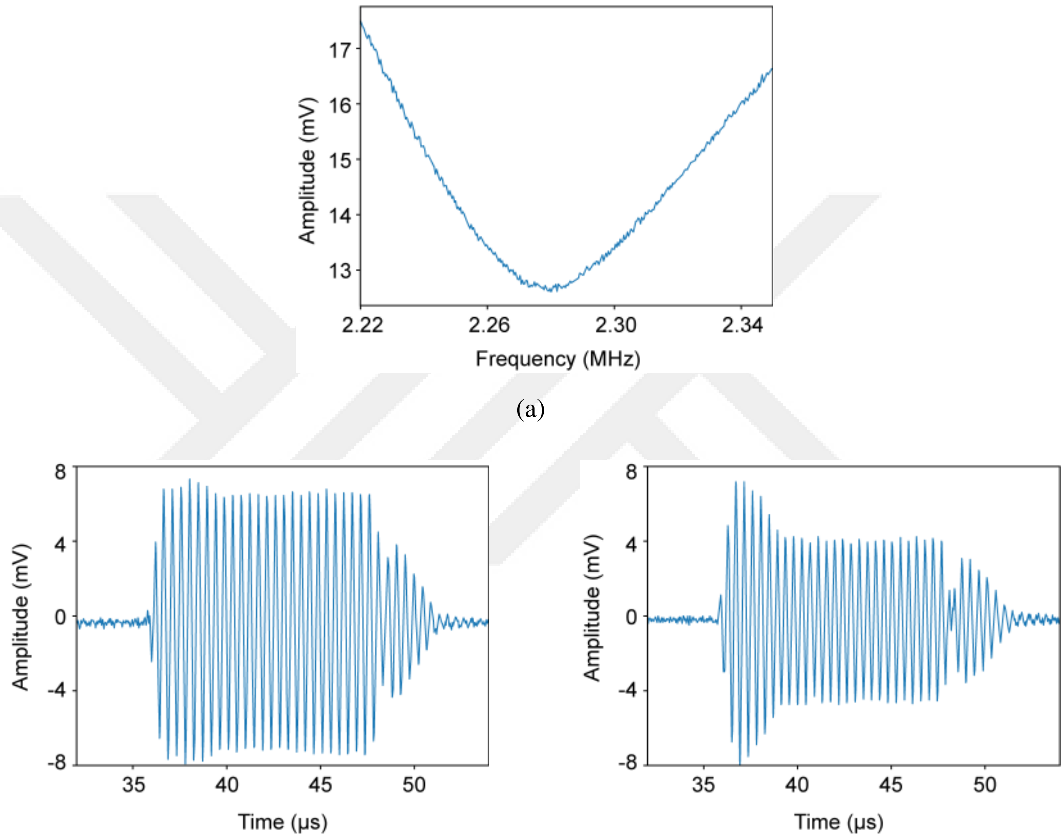

(a) (b) (c)

Figure 3.10: Backscattered waveform evolution for different frequencies. (a) The communication sweep profile of a US antenna, showing a valley at 2.281 MHz. (b) Backscattered waveform at 2.2 MHz and (c) 2.281 MHz.

The raw sweep result outputted by the LIA is often noisy. Since the PUC method relies on the accurate extraction of the valley frequency, any apparent noise must be eliminated. Therefore, the raw signal is post-processed using a Python script and the noise is eliminated by using Gaussian filter, as shown in Figure 3.11.

Although the effects of capacitive and resistive loads were discussed in Sections 2.1 and 2.2, the communication sweeps acquired using the lock-in amplifier may be related

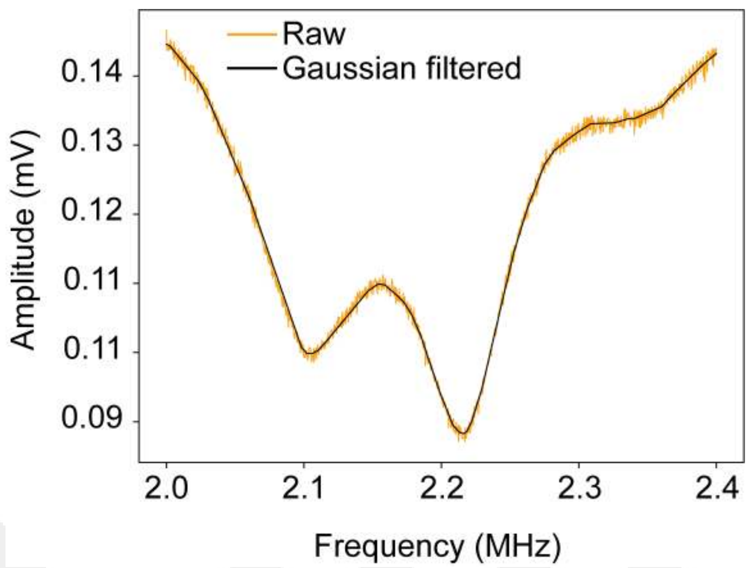

Figure 3.11: Gaussian filter post-processing of an acquired communication sweep profile.

to a completely unrelated phenomenon. Therefore, in order to prove that the valley occurs solely due to the presence of the US antenna, sweep operations were performed with and without the US antenna in front of the interrogator transducer. The resulting sweeper spectrum shows a clear valley when the US antenna is in front of the commercial interrogator transducer. In contrast, when a solid object is placed instead of the antenna, the previously observed valley disappears (Figure 3.12).

Figures 3.13a and 3.13b show the communication sweep results for various capacitive loads connected to the US antenna in parallel. As the load capacitance increases from 0 pF to 120 pF, the spectrum of the received ultrasound waves experiences a shift of 18.56 kHz. The average standard deviation for measurements was calculated as 1.71 kHz. A 2nd order polynomial curve fit reveals a sensitivity of 236 Hz/pF at 0 pF and 62 Hz/pF at 120 pF.

Figure 3.14 shows a violin plot representing the distribution of the measured anti-resonance frequencies of 100 measurements for three different capacitive loads, 0, 50, and 100 pF, showing decent precision.

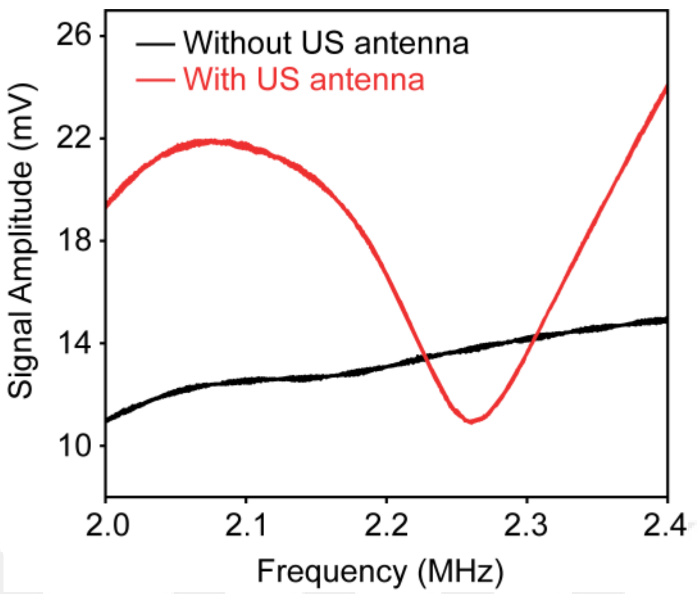

Figure 3.12: Ultrasonic communication sweep results with and without a US antenna in front of the interrogator transducer (n=10).

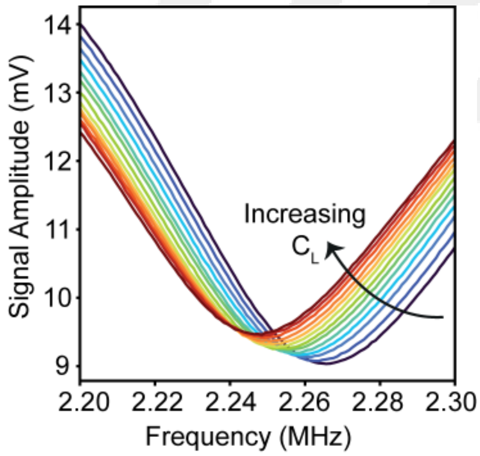

(a)

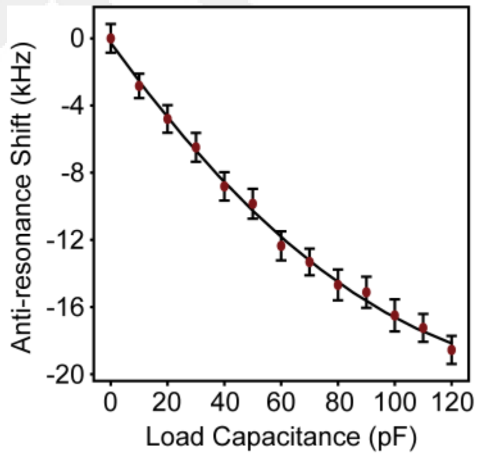

(b)

Figure 3.13: Ultrasonic communication sweep results for various load capacitance values. The sweep results for each load capacitance (a) and the shifts observed with respect to $0pF$ (b) are shown (n=50).

3.4.1 Effect of Distance, Excitation Duration and Amplitude

The PUC method was further analyzed for varying interrogator-antenna distance, excitation length, and signal amplitude. First, the distance between the interrogator transducer and the US antenna was set to the interrogator transducer's focal length.

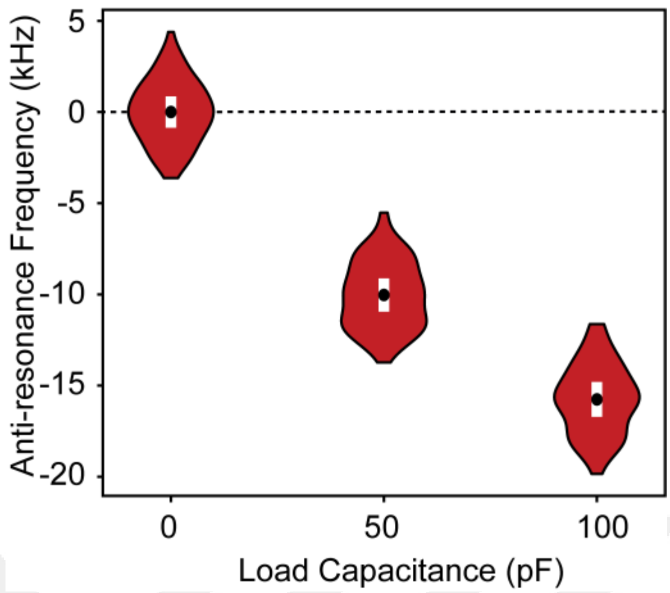

Figure 3.14: Violin plot showing the measurement distribution of the ultrasonic communication system. Black points and white bars show the mean and standard deviation of the measurements, respectively (n=100).

Starting from that position, sweep measurements were performed at two more distances, 5 mm apart each. The results (Figure 3.15) show that distance only slightly affects the communication method, even though it can be entirely compensated since the distance information can be extracted from the time of flight of the pulse-echo measurements.

Moreover, the effect of excitation length (duration) was analyzed (Figure 3.16). As the excitation duration increases, the quality factor of the resulting sweep profile improves. However, the excitation duration cannot be increased without a limit. The distance between the implant (US antenna) and the interrogator transducer is determined by the depth of the targeted deep tissue, and the excitation duration must be less than the pulse-echo time of flight duration so that the transmit and receive phases do not overlap. Unlike excitation duration, the excitation amplitude has no noticeable effect on the performance of the communication method. Figure 3.17 shows the experiment results, comparing the acquired sweeps from using 5 different excitation voltages ranging from 6- to 30-V_{pp}. The results suggest that using voltages as low as 6 V_{pp} introduces noise, which may affect the accuracy and precision of the system.

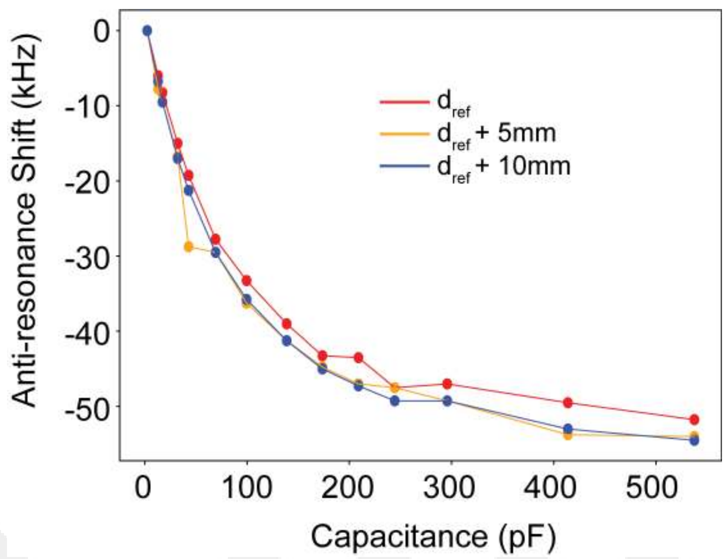

Figure 3.15: The effect of distance between the interrogator transducer and US antenna. The reference distance (d_{ref}) is approximately equal to the focal distance of the interrogator transducer.

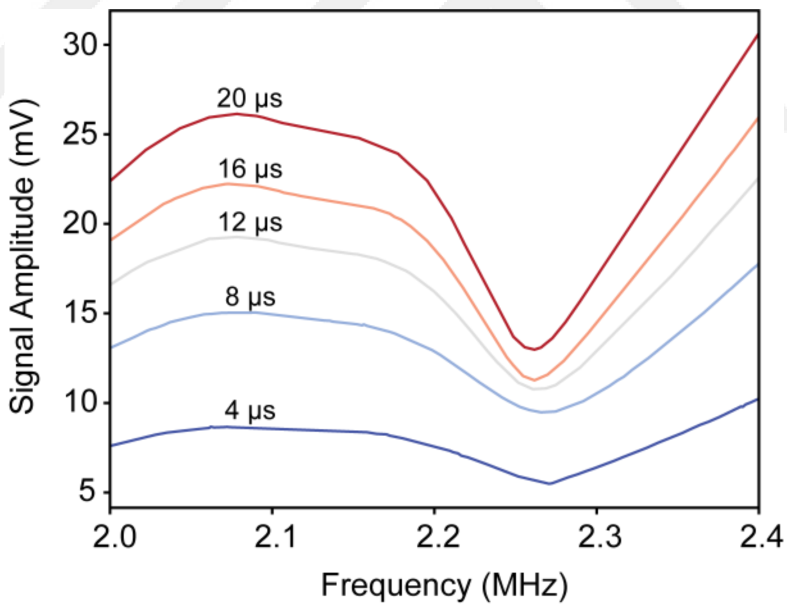

Figure 3.16: The effect of excitation duration. As the excitation duration increases the quality factor of the valley improves but the signal duration is limited by the time of flight of the pulse-echo measurement.

3.4.2 Characterization of the Capacitive and Resistive Effects

In order to understand the source of the communication shifts and to observe the effect of the electrical load impedance, communication sweep measurements were performed

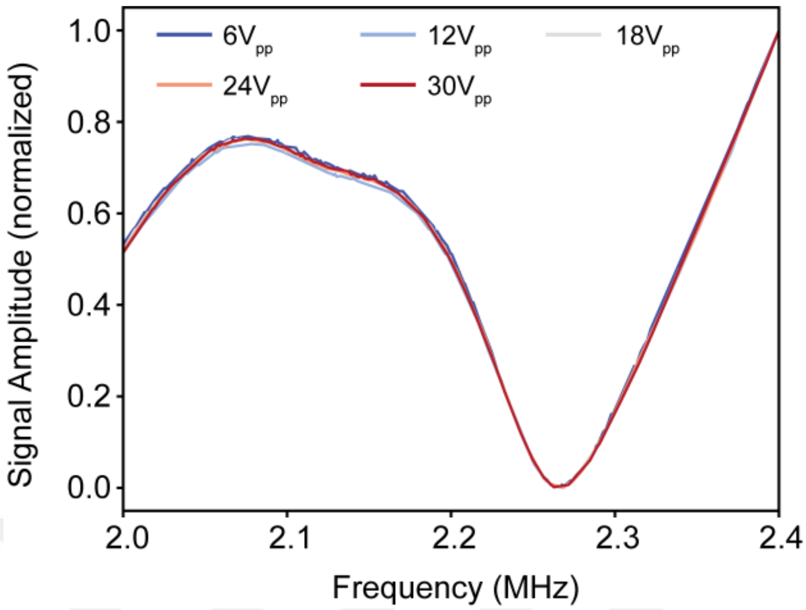

Figure 3.17: The effect of excitation voltage on the performance of the communication method.

while various through-hole resistors were connected to the US antenna and compared against the results of capacitive loads. A 10x10x1 mm^3 US antenna was used for this study.

The raw sweeps and shifts recorded for various parallel capacitive loads are presented in Figure 3.18. The shift curve shows an exponential decrease trend, as expected. However, every electrical component has an impedance. As described in Section 2.2, the role of resistive effects must be analyzed separately to distinguish the individual phenomenon. Therefore, various through-hole resistors were connected to the US antenna. The resulting communication sweeps are displayed in Figure 3.19a. The extracted valley frequencies reveal the shifts, as can be seen in Figure 3.19b. As expected, the frequency at which the acoustic reflection coefficient is minimum shifts only between the resonance and anti-resonance impedances of the US antenna. Here, the impedance of the antenna is approximately 100Ω at its resonance frequency, while its impedance is around 1200Ω at its anti-resonance frequency. At impedances below the resonance impedance and above the anti-resonance impedance, the acoustic reflection coefficient frequency does not experience any shift.

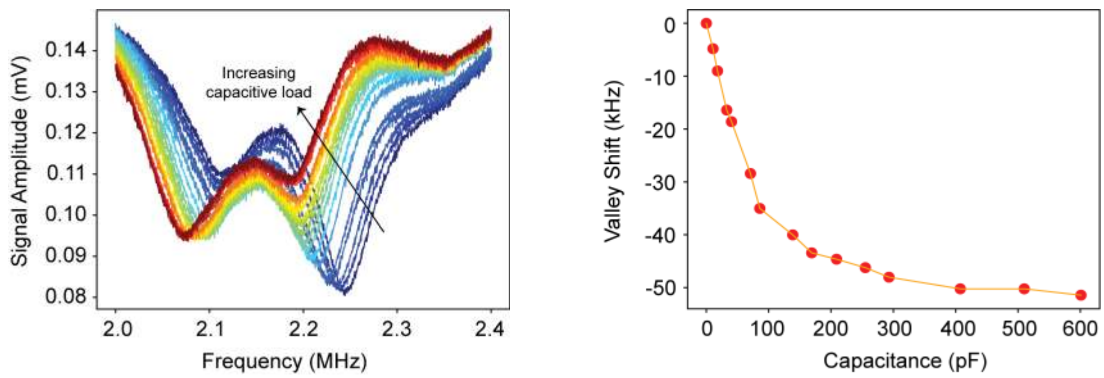

(a) (b)

Figure 3.18: Communication sweep results for varying capacitive loads. (a) shows the communication sweeps and (b) shows the extracted valley frequencies.

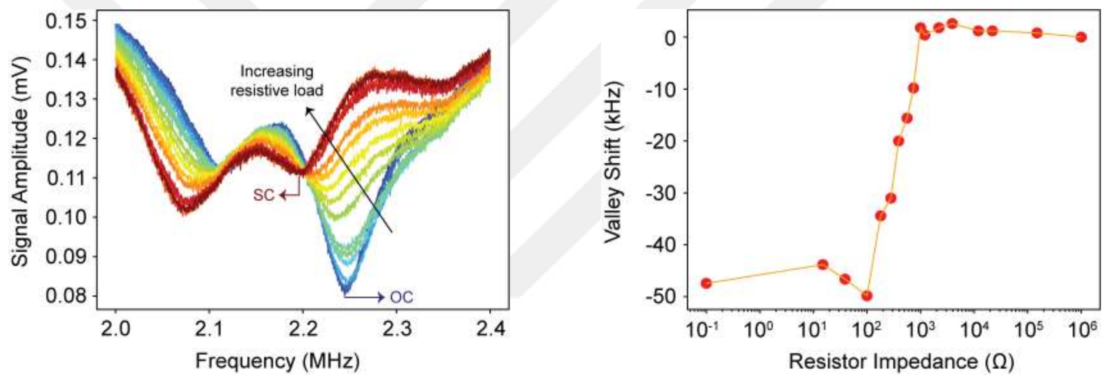

(a) (b)

Figure 3.19: Communication sweep results for varying resistive loads. (a) shows the communication sweeps and (b) shows the extracted valley frequencies.

Although Figures 3.18 and 3.19 show that capacitive and resistive loads cause different behaviors, the capacitive and resistive effects were further compared by calculating the equivalent impedance of the capacitive loads (Figure 3.20).

Furthermore, a test with a combined load was conducted. Communication sweeps were performed while various capacitors and resistors were connected to the US antenna in parallel. Figure 3.21 shows that there is no noticeable effect in the shifts when the parallel resistor has a higher impedance than the anti-resonance impedance of the antenna. However, 600Ω results start to show a decay in the amount of shift, since 600Ω is between the resonance and anti-resonance impedances of the antenna. Finally, when a resistor with

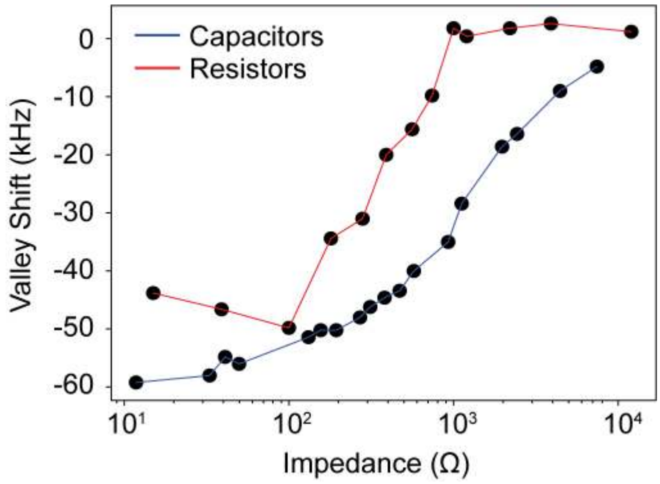

Figure 3.20: Comparison of the valley shifts due to resistive and capacitive effects. The impedance values of the capacitive loads were calculated at 2-MHz.

an impedance close to the resonance impedance of the US antenna is connected, the shift almost completely disappears, since in this condition the frequency of the lowest acoustic reflection coefficient is fixed at the resonance frequency of the US antenna, and hence the anti-resonance shifts caused by the capacitive changes do not translate into valley shifts in the communication sweeps.

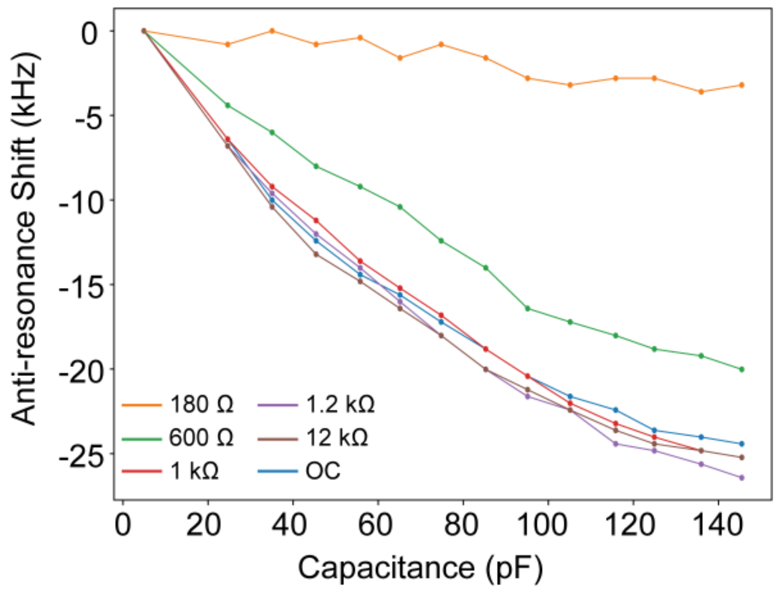

Figure 3.21: Anit-resonance (valley) shifts under combined (capacitive and resistive) load.

3.5 Alternative Excitation Types

Sweeping the frequency range of interest necessitates performing many pulse-echo measurements. For instance, if the desired sweep interval is from 2.1 MHz to 2.3 MHz, 100 frequency points must be used to achieve 2 kHz sweep resolution. Considering that a sufficient amount of time must be allocated between each pulse-echo measurement for the dissipation of the propagating waves, idle time can be around 100 ms (assuming 1 ms burst period). Additionally, the demodulation and post-processing steps of the pulse-echo operation must be taken into account. Therefore, our observations suggest that a 100 frequency point sweep takes approximately 1 second, which yields a communication rate of only 1 Hz. It is possible to increase this rate by improving the post-processing algorithm which can allow the usage of lower sweep points without sacrificing the sensitivity and resolution of the final communication result. However, the method of excitation may also be altered to significantly increase the communication rate.

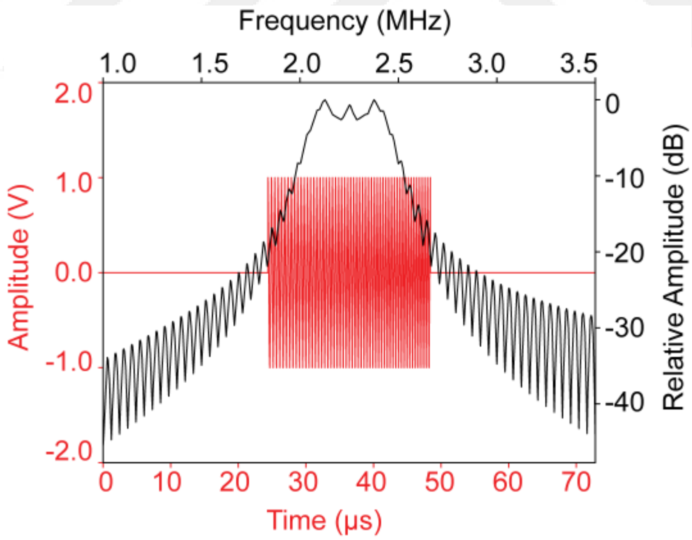

Figure 3.22: An example chirp excitation signal containing frequencies between 2- and 2.5-MHz, and its frequency spectrum.

Instead of performing pulse-echo measurements at individual frequencies in a range, a single excitation waveform containing the whole range can be used for the excitation. Chirp and pulse signals are two examples of such excitation types[69, 70]. Figure 3.22 shows an example chirp signal that contains frequencies between 2- and 2.5-MHz. The

FFT of the waveform reveals that the signal only contains the desired frequency range. Alternatively, Figure 3.23 shows an example pulse signal with a pulse width of 20 ns, and its frequency spectrum. It can be seen that the signal is able to excite a wide range of frequencies. By using chirp or pulse excitation methods, one can extract the anti-

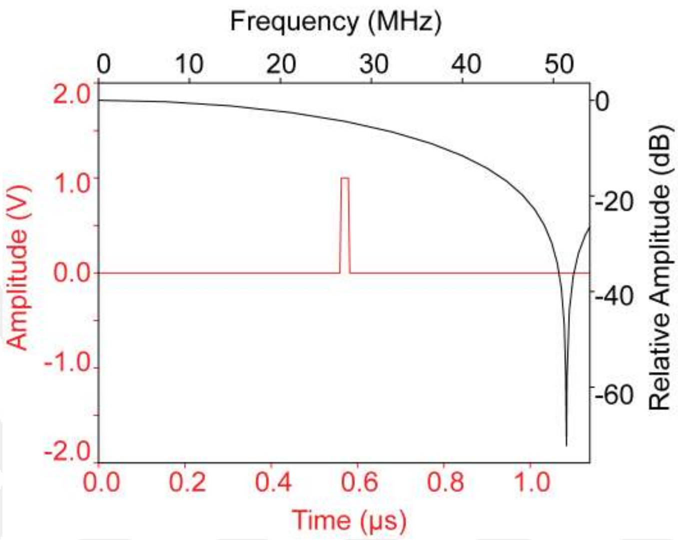

Figure 3.23: An Example pulse excitation signal with a 20 ns pulse width, and its frequency spectrum.

resonance frequency information from a single pulse-echo measurement, increasing the communication rate up to the pulse repetition frequency which is 1 kHz for a burst period of 1 ms, neglecting other hardware-related delays.

In order to investigate the performance of the chirp excitation method, a 3x3x1 mm^3 US antenna was submerged into a distilled water tank, using the same hardware schematic illustrated in Figure 3.8. The arbitrary waveform generator module of the LIA was altered such that it transmits a chirp signal similar to the one displayed in Figure 3.8 the only difference being the excitation type and post-processing algorithm.

A recorded backscattered signal is displayed in Figure 3.24a. As can be seen, the signal amplitude creates a valley even in the time domain. The frequency spectrum of the waveform is displayed in Figure 3.24b, showing the comparison of the regular and zoom FFT algorithms. Moreover, various through-hole capacitors were connected to the US antenna in parallel and the chirp communication was repeated. Similar to the sweep method, an increase in capacitive load resulted in a shift in the valley, as can be seen in Figure 3.24c.

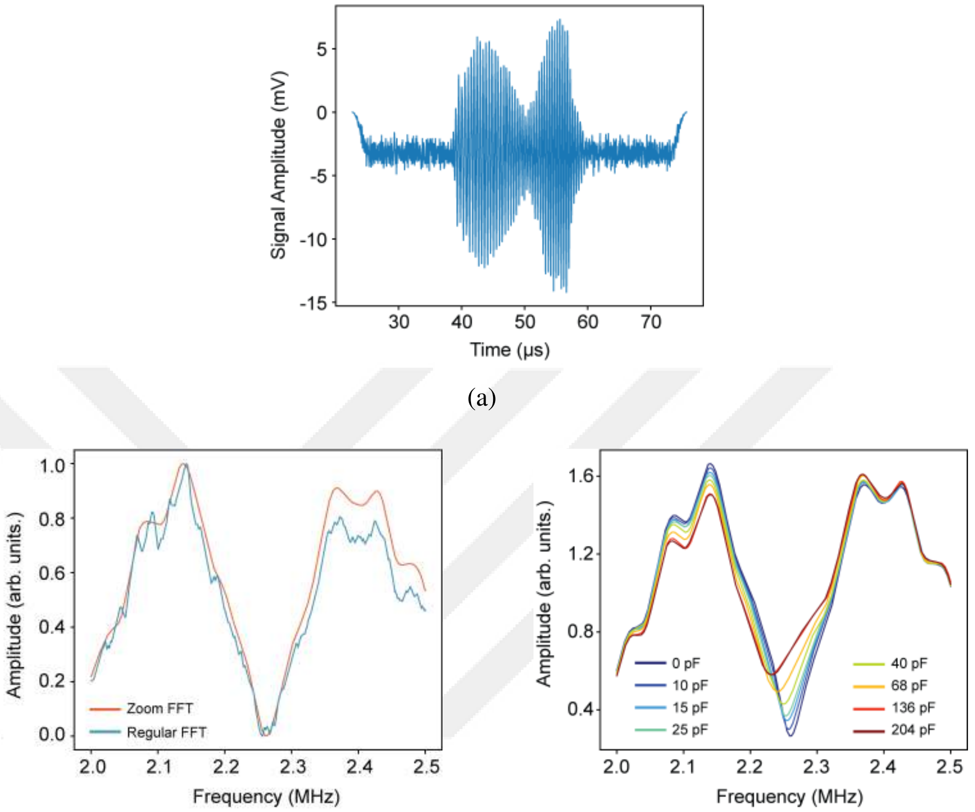

(a) (b) (c)

Figure 3.24: Communication results using chirp excitation. (a) Backscattered chirp signal, showing a clear valley even in time-domain signal. (b) The comparison of the regular and zoom FFT post-processing algorithms. (c) The communication profiles for various through-hole capacitors connected to the US antenna in parallel.

The reason for the adoption of the sweep method was due to the FFT resolution issues associated with the chirp and pulse methods. Therefore, we decided to proceed with the sweep method even though it offers inferior sampling rates.

Chapter 4

IN-VITRO DEMONSTRATION

4.1 Experiment Setup

In order to demonstrate the applicability of the PUC system, a commercial capacitive pressure sensor was integrated with the US antenna, which was then placed in a custom-designed pressure tank. Figure 4.1 shows the schematic of the in-vitro experimental setup and Figure 4.2 shows the optical image of the setup.

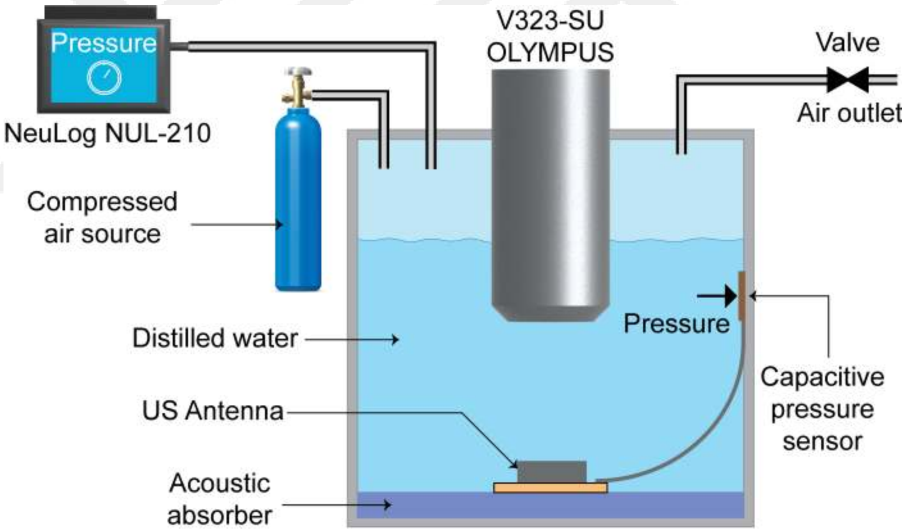

Figure 4.1: Schematic of the in vitro experiment setup.

The pressure tank was constructed from a 15x15x15 cm^3 polycarbonate box and a 3D-printed top cover which houses the air connections and interrogator transducer. The 3D-printed top cover was designed such that it forms a tight fit with the box, and rubber O-rings and a liquid sealant (RTV 300, SIBAX) were used to seal the tank and prevent air leakages.

A total of three air hose connections were designed, one for the air inlet, one for the air outlet, and one for the reference air pressure sensor readings.

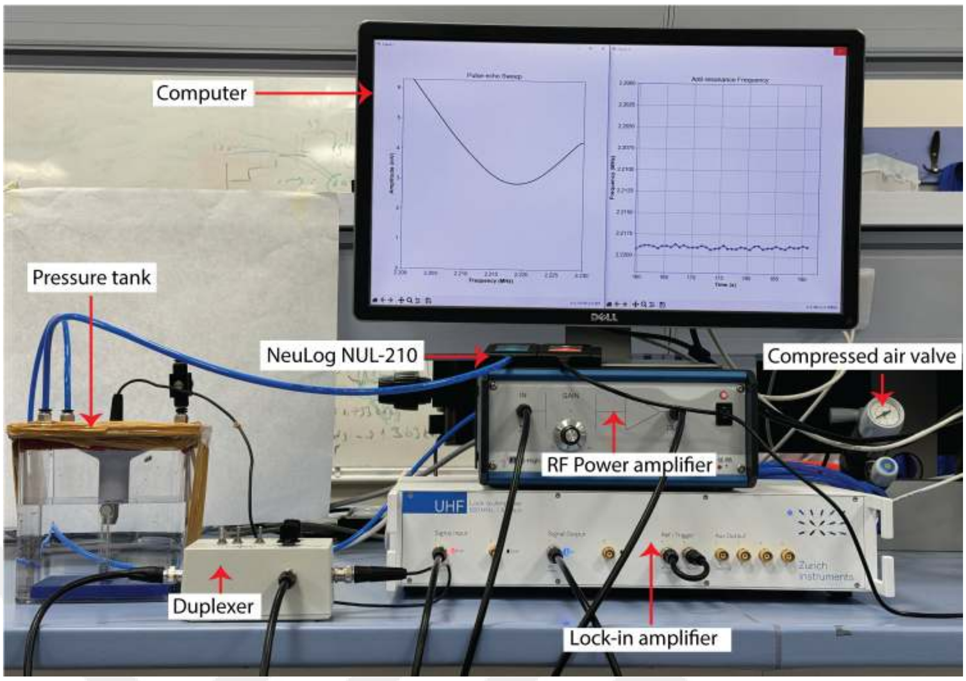

Figure 4.2: Image of the in vitro experiment setup.

The air outlet port of the pressure tank was adjusted such that it allowed at least some airflow. The air inlet was connected to a compressed air source, and the flow rate was controlled manually. The tank was partially filled with distilled water in order to facilitate the ultrasound wave propagation between the interrogator transducer and the US antenna, which were 5 cm apart from each other.

The commercial pressure sensor (FlexiForce A201, Tekscan) was integrated into the fabricated US antenna and the integrated device was placed inside the box such that the US antenna is directly under the interrogator transducer. The sensing area of the commercial pressure sensor was fixed on the box wall.

The input channel of the LIA was connected to the ”TO REC.” port of the duplexer. The output channel of the LIA was connected to the input channel of the RF power amplifier whose output is connected to the input port of the duplexer. The interrogator transducer was directly connected to the duplexer’s out port.

4.2 In-vitro Experiment

The capacitance of the integrated commercial sensor was measured under varying pressure levels (Figure 4.3), showing a sensitivity of approximately 5.83 pF/kPa at pressures below 20 kPa.

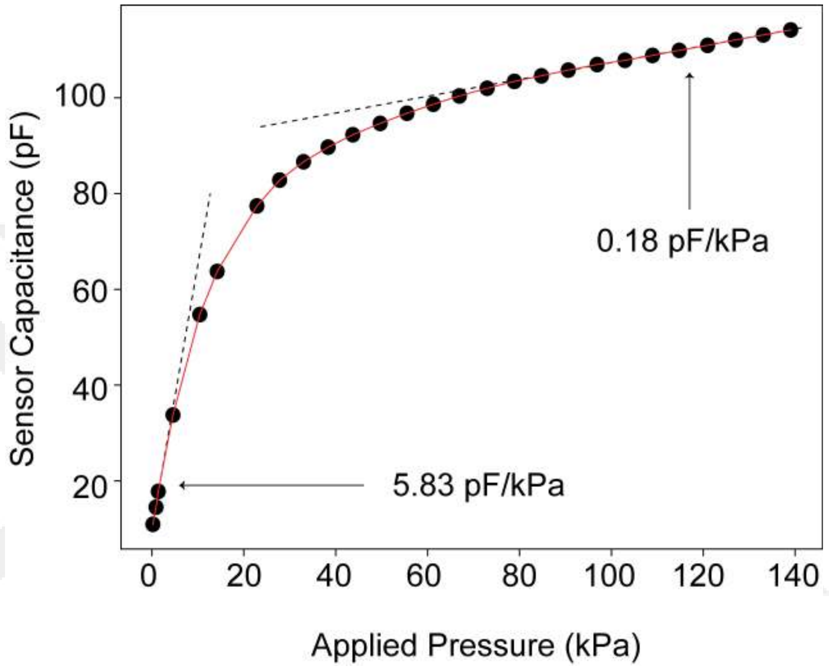

Figure 4.3: The capacitance plot of the integrated capacitive pressure sensor under varying pressure.

Using the integrated system consisting of a US antenna and sensor, the air pressure inside the tank was monitored using the electronics-free PUC method, and was compared to the commercial pressure sensor (NeuLog NUL-210) readings. Figure 4.4a shows the communication sweeps performed at four different pressure levels before any post-processing steps, showing decent separation and precision. Moreover, Figure 4.4b shows the mean and standard deviation of the anti-resonance frequencies extracted from the communication sweeps.

In addition, cyclic air pressure measurement results are presented in Figure 4.5, showing the transient performance of the PUC method. During the transient experiments, the proposed system utilized a sweep resolution of 500 Hz resulting in a sample rate of approximately 1 Hz, limited by the hardware as discussed in Section 3.5.

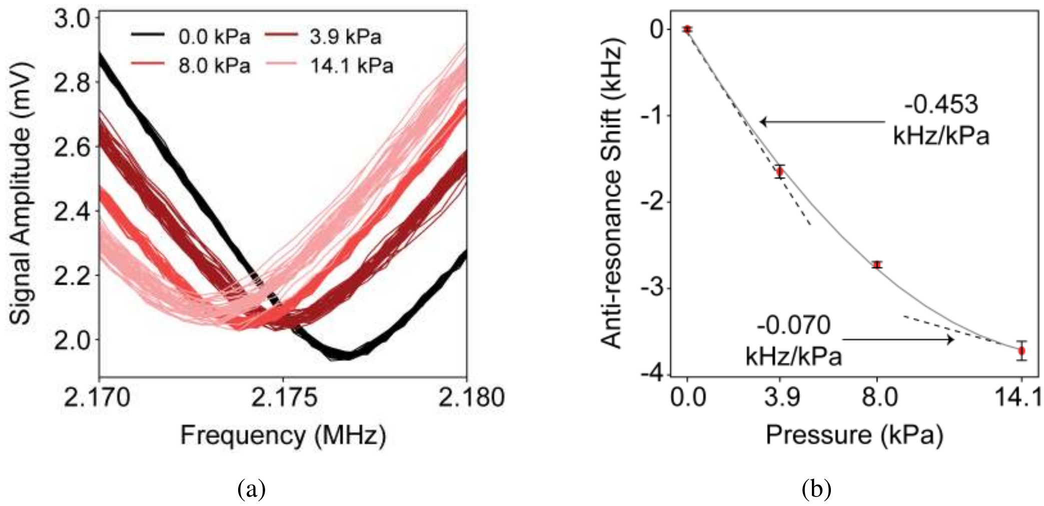

Figure 4.4: In vitro demonstration results. (a) The communication sweeps recorded for four different pressure levels (n=40). (b) The mean and standard deviation of the valley frequencies yielding a sensitivity of approximately -0.453 and -0.070 kHz/kPa, respectively.

Overall, the PUC method results demonstrate decent agreement with the pressure values measured by the commercial sensor.

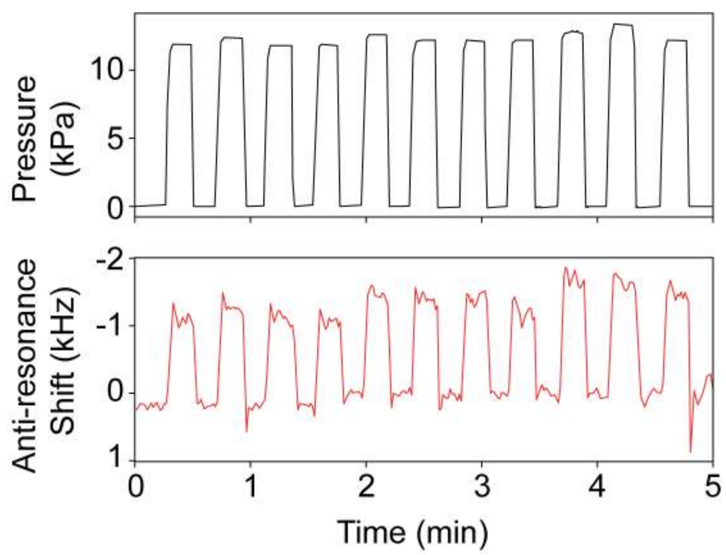

Figure 4.5: Cyclic performance of the communication method. The pressure in the tank was varied manually by controlling the compressed air valve. The communication sweeps were recorded in real time with a sample rate of 1 Hz. The observed anti-resonance shift was slightly less than expected results due to uncontrolled misalignments from pressure fluctuations in the tank.

Chapter 5

CONCLUSION

In this thesis, we presented a simple, wireless, and passive frequency-based ultrasonic communication method for deep tissue sensor implants. The method utilizes ultrasound waves and leverages the changes in the resonance characteristics of the implanted US antenna in order to facilitate communication at greater implantation depths. The system consists of a single piezoceramic US antenna connected to a capacitive sensor in parallel. We demonstrated the performance of the method in vitro at a depth of 5 cm for medically relevant pressures[63, 64, 65, 66] by integrating a commercial capacitive pressure sensor.

Compared to existing technologies that use ultrasound for establishing wireless communication links[34, 35, 36, 37, 38, 39, 40, 41, 42, 43, 44, 45, 47, 46], the PUC method offers several advantages. First, the proposed method features only a single piezoceramic element, used as an ultrasonic antenna, soldered on a flexible conductive substrate. This enables simpler fabrication without needing any microfabrication processes. Second, the PUC system completely eliminates the need for custom-designed integrated circuits and other power-harvesting electronic components, which simplifies the implant design significantly. Finally, the PUC method offers flexibility in terms of sensor integration since any sensor with a capacitive sensing behavior can be used in conjunction with the US antenna.

We observed that the sweep results were affected by the angular and transverse misalignments between the antenna and the interrogator transducer. Therefore, future work will focus on analyzing the misalignment effects and formulating a generalized calibration algorithm that can diminish the misalignment susceptibility. In addition, the US antenna is fabricated using PZT-5H, a material that contains lead. Although biocompatibility is critical for implantable systems, these concerns were not prioritized for this proof-of-concept work. However, lead-free alternatives like KNN[71] can be used to fabricate the US antenna as a future work. Furthermore, the antenna can be miniaturized using microfabrication processes to minimize tissue damage risks during implantation, and the sensor and antenna can be fabricated on the same substrate to achieve a monolithic implantable device. In addition, the fabrication flow involves several manual processes such as PZT alignment and soldering which reduces the reliability and repeatability. Therefore, a pick-and-place machine can be used to align the PZT on the square-cut shape on the PCB substrate, and a wire bonder device can be used to minimize the solder mass left on the top electrode of the PZT.

On the data processing side, the data transfer rates between the computer and the lock-in amplifier formed a bottleneck for the sweep noise since higher data rates result in more accurate demodulated signal profiles. Lastly, the current method offers sampling rates of up to 2 Hz due to the use of the sweep method. By using an alternative interrogation method, such as chirp or pulse excitation, the sampling rate can be increased as high as 1 kHz, limited only by the pulse repetition frequency of the ultrasound excitation. The preliminary study on chirp excitation can be extended to achieve superior communication rates.

As a future work, the equipment used in this thesis can be miniaturized to enable portable or even wearable PUC measurements on demand. The tasks lock-in amplifier performs can be replicated by an electronic board comprised of components such as micro-controller units, high voltage pulsers, mixers etc. As a result, a wearable and portable PCB can be realized with identical capabilities.

Additionally, the antenna can be further characterized mechanically. A Laser Doppler vibrometer and an impedance analyzer can be used to examine the relationship between the electrical and mechanical resonance characteristics of the ultrasonic antenna.

BIBLIOGRAPHY

[1] J. Curie and P. Curie, “Développement par compression de l’électricité polaire dans les cristaux hémièdres à faces inclinées,” *Bulletin de minéralogie*, vol. 3, no. 4, pp. 90–93, 1880.

[2] D. J. Leo, *Engineering analysis of smart material systems*. John Wiley & Sons, 2007.

[3] K. Nakamura, *Ultrasonic transducers: Materials and design for sensors, actuators and medical applications*. Elsevier, 2012.

[4] C. R. Hill, J. C. Bamber, and G. R. ter Haar, *Physical principles of medical ultrasonics*. John Wiley & Sons, 2004.

[5] K. R. Maday, J. B. Hurt, P. Harrelson, and J. Porterfield, “Evaluating postoperative fever,” *JAAPA*, vol. 29, p. 23, 10 2016.

[6] J. Hoffmann, S. P. Mollan, K. Paemeleire, C. Lampl, R. H. Jensen, and A. J. Sinclair, “European headache federation guideline on idiopathic intracranial hypertension,” *The Journal of Headache and Pain*, vol. 19, p. 93, 10 2018.

[7] J. D. Hunter and Z. Damani, “Intra-abdominal hypertension and the abdominal compartment syndrome,” *Anaesthesia*, vol. 59, no. 9, pp. 899–907, 2004. eprint: https://onlinelibrary.wiley.com/doi/pdf/10.1111/j.1365-2044.2004.03712.x.

[8] H. Kobayashi, M. R. Longmire, M. Ogawa, P. L. Choyke, and S. Kawamoto, “Multiplexed imaging in cancer diagnosis: applications and future advances,” *The Lancet Oncology*, vol. 11, pp. 589–595, 6 2010. publisher: Elsevier PMID: 20338808.

[9] S. Bidot, A. M. Saindane, J. H. Peragallo, B. B. Bruce, N. J. Newman, and V. Biousse, "Brain imaging in idiopathic intracranial hypertension," *Journal of Neuro-Ophthalmology*, vol. 35, p. 400, 12 2015.

[10] P. Pelosi, M. Aspesi, C. Gamberoni, D. Chiumello, P. Severgnini, R. Oggioni, G. Tulli, R. Malacrida, and M. Chiaranda, "Measuring intra-abdominal pressure in the intensive care setting," *Intensivmedizin und Notfallmedizin*, vol. 39, pp. 509–519, 9 2002.

[11] M. Abraham and V. Singhal, "Intracranial pressure monitoring," *Journal of Neuroanaesthesiology and Critical Care*, vol. 02, pp. 193–203, 12 2015.

[12] M. Smith, "Monitoring intracranial pressure in traumatic brain injury," *Anesthesia & Analgesia*, vol. 106, p. 240, 1 2008.

[13] R. C. L. Feneley, I. B. Hopley, and P. N. T. Wells, "Urinary catheters: history, current status, adverse events and research agenda," *Journal of Medical Engineering & Technology*, vol. 39, p. 459–470, 11 2015. publisher: Taylor & Francis eprint: https://doi.org/10.3109/03091902.2015.1085600 PMID: 26383168.

[14] R. Hanna and I. I. Raad, "Diagnosis of catheter-related bloodstream infection," *Current Infectious Disease Reports*, vol. 7, pp. 413–419, 12 2005.

[15] R. A. Lange and L. D. Hillis, "Diagnostic cardiac catheterization," *Circulation*, vol. 107, pp. e111–e113, 5 2003. publisher: American Heart Association.

[16] K. H. Dellimore, A. R. Helyer, and S. E. Franklin, "A scoping review of important urinary catheter induced complications," *Journal of Materials Science: Materials in Medicine*, vol. 24, pp. 1825–1835, 8 2013.

[17] E. Bouza, A. Burillo, and P. Muñoz, "Catheter-related infections: diagnosis and intravascular treatment," *Clinical Microbiology and Infection*, vol. 8, pp. 265–274, 5 2002.

[18] C. M. Boutry, L. Beker, Y. Kaizawa, C. Vassos, H. Tran, A. C. Hinckley, R. Pfattner, S. Niu, J. Li, J. Claverie, Z. Wang, J. Chang, P. M. Fox, and Z. Bao, "Biodegradable and flexible arterial-pulse sensor for the wireless monitoring of blood flow," *Nature Biomedical Engineering*, vol. 3, pp. 47–57, 1 2019. publisher: Nature Publishing Group.

[19] S. Rodriguez, S. Ollmar, M. Waqar, and A. Rusu, "A batteryless sensor asic for implantable bio-impedance applications," *IEEE Transactions on Biomedical Circuits and Systems*, vol. 10, pp. 533–544, 6 2016. event-title: IEEE Transactions on Biomedical Circuits and Systems.

[20] R. Herbert, S. Mishra, H.-R. Lim, H. Yoo, and W.-H. Yeo, "Fully printed, wireless, stretchable implantable biosystem toward batteryless, real-time monitoring of cerebral aneurysm hemodynamics," *Advanced Science*, vol. 6, no. 18, p. 1901034, 2019. eprint: https://onlinelibrary.wiley.com/doi/pdf/10.1002/advs.201901034.

[21] S. Hu, H. Chen, S. Jia, X. Xiao, Y. Cao, and W. Wang, "A wireless passive extra-arterial implantable blood pressure monitoring sensing system for rats," *Microsystem Technologies*, vol. 27, pp. 2595–2603, 7 2021.

[22] H. Zhang, P. Gutruf, K. Meacham, M. C. Montana, X. Zhao, A. M. Chiarelli, A. Vázquez-Guardado, A. Norris, L. Lu, Q. Guo, C. Xu, Y. Wu, H. Zhao, X. Ning, W. Bai, I. Kandela, C. R. Haney, D. Chanda, R. W. Gereau, and J. A. Rogers, "Wireless, battery-free optoelectronic systems as subdermal implants for local tissue oximetry," *Science Advances*, vol. 5, p. eaaw0873, 3 2019. publisher: American Association for the Advancement of Science.

[23] C. C. Vassiliou, V. H. Liu, and M. J. Cima, "Miniaturized, biopsy-implantable chemical sensor with wireless, magnetic resonance readout," *Lab on a Chip*, vol. 15, pp. 3465–3472, 8 2015. publisher: The Royal Society of Chemistry.

[24] W. Wang, R. Pradhan, Y. S. Ho, Z. Zhao, Q. Sun, X. Liao, S. Wang, Z. Fang, and Y. Zheng, "Mrc-based double figure-of-eight coil sensor system with triple-mode

operation capability for biomedical applications," *IEEE Sensors Journal*, vol. 21, pp. 14491–14502, 7 2021. event-title: IEEE Sensors Journal.

[25] S.-K. Kang, R. K. J. Murphy, S.-W. Hwang, S. M. Lee, D. V. Harburg, N. A. Krueger, J. Shin, P. Gamble, H. Cheng, S. Yu, Z. Liu, J. G. McCall, M. Stephen, H. Ying, J. Kim, G. Park, R. C. Webb, C. H. Lee, S. Chung, D. S. Wie, A. D. Gujar, B. Vemulapalli, A. H. Kim, K.-M. Lee, J. Cheng, Y. Huang, S. H. Lee, P. V. Braun, W. Z. Ray, and J. A. Rogers, "Bioresorbable silicon electronic sensors for the brain," *Nature*, vol. 530, pp. 71–76, 2 2016. publisher: Nature Publishing Group.

[26] K. Yamagishi, W. Zhou, T. Ching, S. Y. Huang, and M. Hashimoto, "Ultra-deformable and tissue-adhesive liquid metal antennas with high wireless powering efficiency," *Advanced Materials*, vol. 33, no. 26, p. 2008062, 2021. eprint: https://onlinelibrary.wiley.com/doi/pdf/10.1002/adma.202008062.

[27] B. Vennemann, D. Obrist, and T. Rösgen, "A smartphone-enabled wireless and batteryless implantable blood flow sensor for remote monitoring of prosthetic heart valve function," *PLOS ONE*, vol. 15, p. e0227372, 1 2020. publisher: Public Library of Science.

[28] K. Kwon, J. U. Kim, S. M. Won, J. Zhao, R. Avila, H. Wang, K. S. Chun, H. Jang, K. H. Lee, J.-H. Kim, S. Yoo, Y. J. Kang, J. Kim, J. Lim, Y. Park, W. Lu, T.-i. Kim, A. Banks, Y. Huang, and J. A. Rogers, "A battery-less wireless implant for the continuous monitoring of vascular pressure, flow rate and temperature," *Nature Biomedical Engineering*, vol. 7, pp. 1215–1228, 10 2023. publisher: Nature Publishing Group.

[29] T. Wu, J.-M. Redouté, and M. R. Yuce, "A wireless implantable sensor design with subcutaneous energy harvesting for long-term iot healthcare applications," *IEEE Access*, vol. 6, pp. 35801–35808, 2018. event-title: IEEE Access.

[30] B. Silemek, V. Acikel, C. Oto, A. Alipour, Z. G. Aykut, O. Algin, and E. Atalar, "A temperature sensor implant for active implantable

medical devices for in vivo subacute heating tests under mri," *Magnetic Resonance in Medicine*, vol. 79, no. 5, pp. 2824–2832, 2018. eprint: https://onlinelibrary.wiley.com/doi/pdf/10.1002/mrm.26914.

[31] J. Thimot and K. L. Shepard, "Bioelectronic devices: Wirelessly powered implants," *Nature Biomedical Engineering*, vol. 1, no. 3, p. 0051, 2017.

[32] A. L. Chamis, G. E. Peterson, C. H. Cabell, G. R. Corey, R. A. Sorrentino, R. A. Greenfield, T. Ryan, L. B. Reller, and V. G. Fowler, "Staphylococcus aureus bacteremia in patients with permanent pacemakers or implantable cardioverter-defibrillators," *Circulation*, vol. 104, pp. 1029–1033, 8 2001. publisher: American Heart Association.

[33] L. Hall-Stoodley, J. W. Costerton, and P. Stoodley, "Bacterial biofilms: from the natural environment to infectious diseases," *Nature Reviews Microbiology*, vol. 2, pp. 95–108, 2 2004. publisher: Nature Publishing Group.

[34] D. Seo, R. M. Neely, K. Shen, U. Singhal, E. Alon, J. M. Rabaey, J. M. Carmena, and M. M. Maharbiz, "Wireless recording in the peripheral nervous system with ultrasonic neural dust," *Neuron*, vol. 91, pp. 529–539, 8 2016.

[35] S. Ozeri and D. Shmilovitz, "Ultrasonic transcutaneous energy transfer for powering implanted devices," *Ultrasonics*, vol. 50, pp. 556–566, 5 2010.

[36] B. C. Johnson, K. Shen, D. Piech, M. M. Ghanbari, K. Y. Li, R. Neely, J. M. Carmena, M. M. Maharbiz, and R. Muller, "Stimdust: A 6.5mm3, wireless ultrasonic peripheral nerve stimulator with 82% peak chip efficiency," pp. 1–4, 4 2018. ISSN: 2152-3630.

[37] D. K. Piech, B. C. Johnson, K. Shen, M. M. Ghanbari, K. Y. Li, R. M. Neely, J. E. Kay, J. M. Carmena, M. M. Maharbiz, and R. Muller, "A wireless millimetre-scale implantable neural stimulator with ultrasonically powered bidirectional communication," *Nature Biomedical Engineering*, vol. 4, pp. 207–222, 2 2020. publisher: Nature Publishing Group.

[38] C. Shi, T. Costa, J. Elloian, Y. Zhang, and K. L. Shepard, "A 0.065-mm3 monolithically-integrated ultrasonic wireless sensing mote for real-time physiological temperature monitoring," *IEEE Transactions on Biomedical Circuits and Systems*, vol. 14, pp. 412–424, 6 2020. event-title: IEEE Transactions on Biomedical Circuits and Systems.

[39] S. Sonmezoglu, J. R. Fineman, E. Maltepe, and M. M. Maharbiz, "Monitoring deep-tissue oxygenation with a millimeter-scale ultrasonic implant," *Nature Biotechnology*, vol. 39, pp. 855–864, 7 2021. publisher: Nature Publishing Group.

[40] J. Charthad, M. J. Weber, T. C. Chang, and A. Arbabian, "A mm-sized implantable medical device (imd) with ultrasonic power transfer and a hybrid bi-directional data link," *IEEE Journal of Solid-State Circuits*, vol. 50, pp. 1741–1753, 8 2015. event-title: IEEE Journal of Solid-State Circuits.

[41] T. Maleki, N. Cao, S. H. Song, C. Kao, S.-C. Ko, and B. Ziaie, "An ultrasonically powered implantable micro-oxygen generator (imog)," *IEEE Transactions on Biomedical Engineering*, vol. 58, pp. 3104–3111, 11 2011. event-title: IEEE Transactions on Biomedical Engineering.

[42] P. J. Larson and B. C. Towe, "Miniature ultrasonically powered wireless nerve cuff stimulator," pp. 265–268, 4 2011. ISSN: 1948-3554.

[43] L. Maini, V. Genovés, R. Furrer, N. Cesarovic, C. Hierold, and C. Roman, "An in vitro demonstration of a passive, acoustic metamaterial as a temperature sensor with mk resolution for implantable applications," *Microsystems & Nanoengineering*, vol. 10, pp. 1–14, 1 2024. number: 1 publisher: Nature Publishing Group.

[44] J. Zang, Y. Tian, Y. Yang, H. Tang, J. Wang, Y. Cheng, T. Kang, N. Li, M. Zhou, W. Chen, Y. Yu, X. Liu, X. Liu, and L. Xu, "An electronics-free implant for continuous and wireless monitoring of internal tissue strains," 7 2023. ISSN: 2693-5015.

[45] K. Barri, Q. Zhang, I. Swink, Y. Aucie, K. Holmberg, R. Sauber, D. T. Altman, B. C. Cheng, Z. L. Wang, and A. H. Alavi, "Patient-specific self-powered metamaterial implants for detecting bone healing progress," *Advanced Functional Materials*, vol. 32, no. 32, p. 2203533, 2022. eprint: https://onlinelibrary.wiley.com/doi/pdf/10.1002/adfm.202203533.

[46] H. Tang, Y. Yang, Z. Liu, W. Li, Y. Zhang, Y. Huang, T. Kang, Y. Yu, N. Li, Y. Tian, *et al.*, "Injectable ultrasonic sensor for wireless monitoring of intracranial signals," *Nature*, vol. 630, no. 8015, pp. 84–90, 2024.

[47] S. Mutlu, A. Aghakhani, and M. Sitti, "Piezo capsule: Ultrasonic way of wireless pressure measurement," *Advanced Intelligent Systems*, vol. 4, no. 10, p. 2200125, 2022. eprint: https://onlinelibrary.wiley.com/doi/pdf/10.1002/aisy.202200125.

[48] S. Sharma, C.-A. Lernoud, B. Fain, R. Othmen, V. Bouchiat, B. Yvert, and C. Hébert, "Graphene solution-gated field-effect transistor for ultrasound-based wireless and battery-free biosensing," *Advanced Materials Technologies*, vol. 8, no. 15, p. 2300163, 2023.

[49] I. of Electrical and E. Engineers, *ANSI/IEEE Std 176-1987: IEEE Standard on Piezoelectricity*. IEEE, 1988.

[50] M. Guan and W. Liao, "On the equivalent circuit models of piezoelectric ceramics," *Ferroelectrics*, vol. 386, no. 1, pp. 77–87, 2009.

[51] V. Matko and M. Milanovič, "Detection principles of temperature compensated oscillators with reactance influence on piezoelectric resonator," *Sensors*, vol. 20, no. 3, p. 802, 2020.

[52] C.-H. Hong, H.-P. Kim, B.-Y. Choi, H.-S. Han, J. S. Son, C. W. Ahn, and W. Jo, "Lead-free piezoceramics–where to move on?," *Journal of Materiomics*, vol. 2, no. 1, pp. 1–24, 2016.

[53] C. Papageorgiou and T. Laopoulos, "Modification of resonance characteristics of ultrasonic transducers by the driving circuit," *mH*, vol. 1, no. 2, p. V1, 2003.

[54] J.-Y. Park and J.-W. Choi, "Electronic circuit systems for piezoelectric resonance sensors," *Journal of The Electrochemical Society*, vol. 167, no. 3, p. 037560, 2020.

[55] T. C. Chang, *Design and Characterization of Wireless Implant Systems with Ultrasonic Power and Data Links*. Stanford University, 2019.

[56] W. P. Mason, "Electromechanical transducers and wave filters," *(No Title)*, 1948.

[57] M. Castillo, P. Acevedo, and E. Moreno, "Klm model for lossy piezoelectric transducers," *Ultrasonics*, vol. 41, no. 8, pp. 671–679, 2003.

[58] M. Redwood, "Transient performance of a piezoelectric transducer," *The journal of the acoustical society of America*, vol. 33, no. 4, pp. 527–536, 1961.

[59] W. M. Leach, "Controlled-source analogous circuits and spice models for piezoelectric transducers," *IEEE Transactions on ultrasonics, ferroelectrics, and frequency control*, vol. 41, no. 1, pp. 60–66, 1994.

[60] A. Allam, A. Bhardwaj, K. Sabra, and A. Erturk, "Piezoelectric transducer design and impedance tuning for concurrent ultrasonic power and data transfer," in *Active and Passive Smart Structures and Integrated Systems XVI*, vol. 12043, pp. 84–103, SPIE, 2022.

[61] A. Allam, K. Sabra, and A. Erturk, "Piezoelectric transducer design for simultaneous ultrasonic power transfer and backscatter communication," *Smart Materials and Structures*, vol. 31, no. 9, p. 095003, 2022.

[62] R. Wang, E. Tang, G. Yang, and Y. Han, "Experimental research on dynamic response of pzt-5h under impact load," *Ceramics International*, vol. 46, no. 3, pp. 2868–2876, 2020.

[63] M. Czosnyka and J. D. Pickard, “Monitoring and interpretation of intracranial pressure,” *Journal of Neurology, Neurosurgery & Psychiatry*, vol. 75, no. 6, pp. 813–821, 2004.

[64] M. L. Malbrain and D. H. Deeren, “Effect of bladder volume on measured intravesical pressure: a prospective cohort study,” *Critical care*, vol. 10, pp. 1–6, 2006.

[65] N. Galie, M. M. Hoeper, M. Humbert, A. Torbicki, J.-L. Vachiery, J. A. Barbera, M. Beghetti, P. Corris, S. Gaine, J. S. Gibbs, *et al.*, “Guidelines for the diagnosis and treatment of pulmonary hypertension: the task force for the diagnosis and treatment of pulmonary hypertension of the european society of cardiology (esc) and the european respiratory society (ers), endorsed by the international society of heart and lung transplantation (ishlt),” *European heart journal*, vol. 30, no. 20, pp. 2493–2537, 2009.

[66] S. J. Mubarak, C. Owen, A. Hargens, L. Garetto, and W. Akeson, “Acute compartment syndromes: diagnosis and treatment with the aid of the wick catheter.,” *JBJS*, vol. 60, no. 8, pp. 1091–1095, 1978.

[67] V. M. do Nascimento, V. L. d. S. N. Button, J. M. Maia, E. T. Costa, and E. J. V. Oliveira, “Influence of backing and matching layers in ultrasound transducer performance,” in *Medical Imaging 2003: Ultrasonic Imaging and Signal Processing*, vol. 5035, pp. 86–96, SPIE, 2003.

[68] R. E. McKeighen, “Design guidelines for medical ultrasonic arrays,” in *Medical imaging 1998: Ultrasonic transducer engineering*, vol. 3341, pp. 2–18, SPIE, 1998.

[69] J. E. Michaels, S. J. Lee, A. J. Croxford, and P. D. Wilcox, “Chirp excitation of ultrasonic guided waves,” *Ultrasonics*, vol. 53, no. 1, pp. 265–270, 2013.

[70] Y. Onykiienko, O. Batina, G. Vlasyuk, V. Shvaichenko, A. Mitsukova, and O. Marchenko, “The selection of the test pulse duration for a shock excitation

study of ultrasonic transducers," in *2020 IEEE 40th International Conference on Electronics and Nanotechnology (ELNANO)*, pp. 499–502, IEEE, 2020.

[71] J. F. Hou, M. O. G. Nayeem, K. A. Caplan, E. A. Ruesch, A. Caban-Murillo, E. Criado-Hidalgo, S. B. Ornellas, B. Williams, A. A. Pearce, H. E. Dagdeviren, *et al.*, "An implantable piezoelectric ultrasound stimulator (impuls) for deep brain activation," *Nature Communications*, vol. 15, no. 1, p. 4601, 2024.